(4)

AFGL-TR-89-0063

Application of Transilient Turbulence Theory to Mesoscale Numerical Weather Forecasting

William H. Raymond
Roland B. Stull

University of Wisconsin
CIMSS/Department of Meteorology
Madison, WI 53706

February 1989

CS

Final Report
20 February 1987-20 February 1989

APPROVED FOR PUBLIC RELEASE; DISTRIBUTION UNLIMITED

AIR FORCE GEOPHYSICS LABORATORY
AIR FORCE SYSTEMS COMMAND
UNITED STATES AIR FORCE
HANSCOM AIR FORCE BASE, MASSACHUSETTS 01731-5000

This technical report has been reviewed and is approved for publication.

George Modica
GEORGE MODICA
Contract Manager

Donald A Chisholm
DONALD A. CHISHOLM, Chief
Atmospheric Prediction Branch

FOR THE COMMANDER

Robert A. McClatchey
ROBERT A. McCLATCHEY, Director
Atmospheric Sciences Division

This report has been reviewed by the ESD Public Affairs Office (PA) and is releasable to the National Technical Information Service (NTIS).

Qualified requestors may obtain additional copies from the Defense Technical Information Center. All others should apply to the National Technical Information Service.

If your address has changed, or if you wish to be removed from the mailing list, or if the addressee is no longer employed by your organization, please notify AFGL/DAA, Hanscom AFB, MA 01731. This will assist us in maintaining a current mailing list.

Do not return copies of this report unless contractual obligations or notices on a specific document require that it be returned.

Unclassified
SECURITY CLASSIFICATION OF THIS PAGE

REPORT DOCUMENTATION PAGE

1a. REPORT SECURITY CLASSIFICATION
Unclassified

1b. RESTRICTIVE MARKINGS

2a. SECURITY CLASSIFICATION AUTHORITY

2b. DECLASSIFICATION / DOWNGRADING SCHEDULE

3. DISTRIBUTION / AVAILABILITY OF REPORT
Approved for public release;
Distribution unlimited

4. PERFORMING ORGANIZATION REPORT NUMBER(S)

5. MONITORING ORGANIZATION REPORT NUMBER(S)
AFGL-TR-89-0063

6a. NAME OF PERFORMING ORGANIZATION
University of Wisconsin

6b. OFFICE SYMBOL *(If applicable)*

7a. NAME OF MONITORING ORGANIZATION
Air Force Geophysics Laboratory

6c. ADDRESS *(City, State, and ZIP Code)*
CIMSS/Department of Meteorology
Madison, WI 53706

7b ADDRESS *(City, State, and ZIP Code)*
Hanscom AFB
Massachusetts 01731-5000

8a. NAME OF FUNDING / SPONSORING ORGANIZATION

8b. OFFICE SYMBOL *(If applicable)*

9. PROCUREMENT INSTRUMENT IDENTIFICATION NUMBER
F19628-87-K-0035

8c. ADDRESS *(City, State, and ZIP Code)*

10. SOURCE OF FUNDING NUMBERS

PROGRAM ELEMENT NO.	PROJECT NO.	TASK NO.	WORK UNIT ACCESSION NO
62101F	6670	10	DB

11. TITLE *(Include Security Classification)*
Application of Transilient Turbulence Theory to Mesoscale Numerical Weather Forecasting

12. PERSONAL AUTHOR(S)
William H. Raymond; Roland B. Stull

13a. TYPE OF REPORT
FINAL

13b. TIME COVERED
FROM 2/20/87 TO 2/20/89

14. DATE OF REPORT *(Year, Month, Day)*
1989 February 20

15. PAGE COUNT
74

16. SUPPLEMENTARY NOTATION

17. COSATI CODES

FIELD	GROUP	SUB-GROUP

18. SUBJECT TERMS *(Continue on reverse if necessary and identify by block number)*
Clear Air Turbulence (CAT)
Turbulence parameterization
Boundary layer
Surface fluxes

19. ABSTRACT *(Continue on reverse if necessary and identify by block number)*

A transilient turbulence parameterization has been inserted into the Penn State/NCAR regional three dimensional mesoscale numerical model. Transilient turbulence parameterizes both boundary layer and clear air turbulence (CAT). The new transilient turbulence scheme replaces separate formulations of the boundary layer parameterization, dry convective adjustment, cumulus parameterization and horizontal diffusion. A new surface layer flux formulation that is compatible with the transilient turbulence parameterization has also bee installed. Additionally a sixth order implicit tangent filter has been inserted to remove numerical noise. This separation of the turbulence physics from numerical stability considerations gives us an opportunity to examine the mixing process in greater detail.

We compared forecasts from our revised model with the standard Penn State/NCAR model formulation, which has a Blackadar boundary layer and fourth order K theory horizontal diffusion. Forecasts using both Kuo cumulus parameterization and explicit cloud convective representations have been made with this standard model utiling the OSCAR IV and CAPTEX

20. DISTRIBUTION / AVAILABILITY OF ABSTRACT
☐ UNCLASSIFIED/UNLIMITED ☐ SAME AS RPT. ☐ DTIC USERS

21. ABSTRACT SECURITY CLASSIFICATION
Unclassified

22a. NAME OF RESPONSIBLE INDIVIDUAL
George Modica

22b. TELEPHONE *(Include Area Code)*

22c. OFFICE SYMBOL
GL/LYP

DD FORM 1473, 84 MAR

83 APR edition may be used until exhausted.
All other editions are obsolete.

SECURITY CLASSIFICATION OF THIS PAGE
Unclassified

(continuation of block 19)

data sets. Comparisons between the control and the transilient turbulence approach are used to highlight the role of turbulence and its affect on the overall forecast. Verifying station radiosonde reports and analysis are the final authority on the accuracy of the forecasts.

Our results highlight the role of turbulence and its effect on the overall forecast. With the new turbulence parameterization we obtain a significant positive benefit in the boundary-layer forecasts, in turbulence at higher altitudes, and in the omega fields and area precipitation rates that now exhibit a diurnal cycle with a nocturnal maximum characteristic of mesoscale convective weather systems. Turbulence is found to be sensitive to various feedback processes that modulate convection.

[illegible] Turbulence

Surface fluxes, [illegible]

Contents

1. Introduction

The parameterization of turbulence in meso- and synoptic-scale numerical weather prediction (NWP) models is often accomplished by packaging together a large number of highly-specialized empirical approximations (Anthes, 1983). Some of these components handle the boundary layer, some model clear air turbulence aloft, and others approximate moist convection . Yet, these all parameterize the same one physical phenomenon — turbulence.

For example, the Penn State/NCAR mesoscale model (Anthes et al., 1987) uses K-theory vertical diffusion, Blackadar mixed-layer parameterization, bulk neutral and stable boundary layer parameterizations, dry convective adjustment, Kuo cumulus parameterization, and fourth-order Smagorinsky horizontal diffusion. Since many of these schemes are applied to the same grid points within the model, complex interactions can occur between the parameterizations. To add to the confusion, some of these schemes are "tuned" above realistic levels to damp numerical noise.

Our hypothesis is that numerical weather forecasts can be improved when one unified turbulence-closure approximation is utilized for the whole model domain at all times, instead of using the collection of specialized empirical approximations. This approach also requires that we divorce the parameterization of the physics of turbulence from the nonphysical smoothing necessary for numerical stability. In this paper, we use transilient turbulence theory (TT) as the unified turbulence scheme, and a 6th-order implicit tangent filter for numerical stability. The details of TT are discussed in section 2.

We selected as a host model the version of the Penn State/NCAR three-dimensional hydrostatic primitive equation limited-area mesoscale prediction model having fifteen vertical sigma levels (Anthes and Warner, 1978). Fig 1 is a schematic showing that momentum, temperature and moisture variables are defined at the half-sigma level, while vertical velocity is defined on the full sigma levels (Anthes et al., 1987). In this model the horizontal grid included 61 x 46 points on a Lambert conformal mapping using a horizontal grid spacing of $\Delta x = \Delta y = 80$ km. The time step is 120 s. Other model configurations include a nudging horizontal boundary condition and a two layer surface slab formulation.

Although rarely stated in the open literature, most modelers will admit that the various parameterizations that compose a mesoscale model are intertwined in complex ways. Changing or tuning the parameters of one parameterization affect the success of the other parameterizations in the model. By changing to one unified turbulence theory, we hope to avoid that problem. While we were untangling and removing the myriad small specialized turbulence parameterizations, we discovered an improper application of similarity theory for the estimation of surface fluxes. Our corrected surface-flux scheme that incorporates a thin nonturbulent viscous sublayer is discussed in section 3.

To remove the numerical noise such as is usually present in a finite-difference-type of mesoscale model, a 6th-order implicit tangent filter (Raymond, 1988) is installed. This filter is very selective and enables numerical noise between 2Δx and 4Δx to be removed without significantly altering meaningful meteorological scales. Thus, numerical stability is independent of the turbulence parameterization scheme. Details are discussed in section 4.

Several 72 h forecasts have been run and verification made for the OSCAR IV (0000 UTC 22 April to 0000 UTC 25 April, 1981, prepared by NCAR, see Errico and Baumhefner, 1987) and the CAPTEX (1200 UTC 24 September to 1200 UTC 27 September, 1983, prepared by NCAR) data sets. The former data set represents a spring-time frontal situation in which cyclonic-frontogenic activity is located initially over the Dakotas and an upper-level trough exists just to its west. This system propagates eastward and intensifies, but several small scale waves are also present (Errico and Baumhefner, 1987). The latter data set has been used to examine long-range transport and dispersion of pollution (Kao and Yamada, 1988). During this time period high pressure dominated most of the United States but organized mesoscale convection is present. Forecast results are presented in Section 5.

2. Transilient turbulence

Turbulence is a small-scale phenomenon for which the horizontal structure cannot be resolved in large or mesoscale weather forecast models, but which affects the overall forecasts. Convective events originate from, and are continually fueled by, small scale buoyant plumes associated with boundary-layer processes. The problem that faces the modeler is how to parameterize these turbulent motions within the constraints of time, money and computer power, while at the same time resolving scales many magnitudes larger.

The modelling of turbulence in the boundary layer and in the atmosphere above remains one of the more difficult problems in the atmospheric sciences. Sometimes turbulence and diffusion have been construed as the same process. In reality the processes involve different time and space scales and are physically different. The first attempts to model turbulence (Boussinesq, 1877) took the diffusive formulation for the molecular viscosity of air, enhanced it, and called it an eddy viscosity. By specifying the eddy-diffusion coefficient in terms of known variables, the hydrodynamical equations of motion can be closed and solved. Attempts to find suitable parameterizations for the eddy viscosity based on bulk or large scale variables has occupied a predominant role in early meteorological boundary-layer research. Following upon Boussinesq's constant eddy viscosity and Prandtl's (1925) mixing-length theory, many complicated turbulence models have been proposed. In addition to K theory's first-order closure scheme (Louis, 1979) there are higher-order closure formulations (Zeman, 1981; Wyngaard, 1982; Mellor and Yamada, 1982; Andre, et al., 1987) and spectral theories (Heisenberg, 1948) for turbulence. Unfortunately, the intrinsically nonlocal nature of atmospheric turbulence makes it difficult to apply these local approximations without violating the laws of thermodynamics (e.g., heat flowing from cold to hot, implied by negative K).

In this study we turn our attention to the newly developed transilient turbulence parameterization (Stull, 1984). The nonlocal transilient turbulence parameterization has been compared with the above mentioned local approaches by Stull (1984, 1986) and to turbulent adjustment procedures by Stull and Hasegawa (1984). In many one dimensional tests (Stull and Driedonks, 1987; Stull and Kraus, 1987) this new formulation has yielded outstanding results.

a. The nonlocal nature of turbulence

Turbulence in the atmosphere is not like diffusion, but is more like advection. Blobs or parcels of air are bodily moved across finite distances by eddies of varying sizes, before the parcels (or portions of them) mix with their surroundings. This picture is particularly valid for both boundary-layer convection and convective clouds within the troposphere. For statically stable air, the same picture is valid, although the dominant eddies are usually smaller. Thus, a desirable feature of turbulence parameterizations for numerical weather forecast models is that mixing across all relevant scales be adequately described.

The concept of mixing across finite distances is embodied in a nonlocal first-order closure scheme called transilient turbulence theory (TT). The word "transilient" is based on a latin word meaning "jump over", to convey the advective rather than diffusive nature of TT. For a 1-D column of grid points, there is a matrix $[c_{ij}]$ of mixing coefficients (transilient coefficients) that describe how much air arriving at grid box i came from box j during timestep Δt. Grid points i and j can represent immediate neighbors, or they can be points separated in space (see Fig 2). Thus, the full range of resolvable scales can be represented. In Fig 2b, the curved arrow represents a mixing process, which is the net effect of a superposition of actual eddies that contribute to mixing between the two grid points during timestep Δt. Similar representations can be made in the horizontal.

Measurements of the transilient matrix have been made by Ebert et al. (1989) for the case of free convection in the boundary layer, using equally-spaced grid points. They ran a large-eddy simulation model and injected tracers to track the sources and destinations of all the air within the model. It was not surprising that they found all scales of motion to be important to vertical mixing, not just the small-scales modeled by traditional K-theory. In addition, they found that the matrix is asymmetric for unstable boundary layers. The physical interpretation of any transilient matrix is discussed in detail by them.

b. Implementation of turbulent mixing

Implementation of this scheme into a 1-D forecast model (or into any column of a 3-D model) requires parameterization of the transilient matrix. The parameterization should be able to respond to changes of the mean state caused by the various body forcings (radiation, condensation, Coriolis force, etc.) and boundary conditions (surface heat flux, drag, etc.).

The earliest parameterizations (Berkowicz and Prahm, 1979) assumed a fixed spectrum of turbulence that was not particularly responsive to changes in the mean state. Later, a responsive parameterization was developed by Stull (1984) based on a nonlocal Richardson number, but it did not perform well for arbitrary situations such as radiative cooling at cloud top within the model domain. More recently, Stull and Driedonks (1987) developed a responsive parameterization based on a nonlocal approximation to the turbulence kinetic equation that gave realistic forecasts for unstable, neutral, stable, and cloudy boundary layers. Although this scheme yields only symmetric transilient matrices, it is very robust and automatically satisfies conservation of mass and state. However, the parameterized turbulence is biased to generate the most intense mixing at the lower grid points, which can be corrected as is discussed later.

The responsive parameterizations require that there be some instability to respond to. In addition, a 3-D model requires both horizontal and vertical mixing. Thus, each model forecast timestep must be split into five parts: (i) application to all grid points of all (nonturbulent) boundary conditions and body forcings including dynamics and thermodynamics that could alter or destabilize the flow; (ii) computation of a transilient matrix for vertical mixing for each column of grid points based on this destabilized mean state; (iii) vertical mixing of all state variables in each column based on the computed transilient matrix; (iv) computation of horizontal mixing potentials for each column; and (v) horizontal mixing of all state variables. The procedure is first do step (i) over the whole 3-D domain, next do steps (ii) and (iii) for each column, and finally do steps (iv) and (v).

Step (i) is conducted using the existing physics of the host model, with the exception that all turbulence-related effects are excluded. In the Penn State/NCAR model, we removed vertical K-theory diffusion, Smagorinsky's horizontal diffusion, dry convective adjustment, Kuo subgrid cumulus parameterization, and all the boundary layer parameterizations. Note that the flux of heat, moisture, and momentum between the ground and the air is not a turbulent process (unless the ground begins to dance), and hence that parameterization is retained (see Section 3).

The net effect of step (i) is to split each timestep into (at least) two parts: the nonturbulent-forcing part that incorporates all the other physics, followed by the turbulence part. At the beginning of any timestep, let the state of air within any one column of grid points be $S_i(t)$, where S_i represents moisture, temperature, or momentum-component values at each grid point i within the column. After applying the physics of step (i), define the altered state as $S_i'(t)$.

c. Vertical mixing

For step (ii), we start with the 1-D approach of Stull and Driedonks (1987) to determine the transilient matrix for any one column of grid points. The wind speed differences $[(\Delta U)_{ij}$ and $(\Delta V)_{ij}]$ and virtual potential temperature difference $[(\Delta\theta_v)_{ij}]$ between each pair (i,j) of grid points within the column determines a mixing potential (Y_{ij}) between those points:

$$Y_{ji} = Y_{ij} = \frac{T_o \Delta t}{(\Delta z)_{ij}^2} \left[(\Delta U)_{ij}^2 + (\Delta V)_{ij}^2 - \frac{g\ (\Delta\theta_v)_{ij}\ |\Delta z|_{ij}}{R_c\ \theta_{vi}} \right] - \frac{D\,\Delta t}{T_o} \qquad (1)$$

for $i \neq j$, g is gravitational acceleration, and where $(\Delta\theta_v)_{ij}$ is negative if the lower grid point is warmer than the higher point. The distance between pairs of grid points (i.e., between the centers of the grid boxes) is Δz_{ij} as sketched in Fig 2b. The above equation is also valid for unequally-spaced grid points. Note that a typographical error in (6) of Stull and Driedonks (1987) resulted in the omission of the Δz_{ij} factor in the last term in square brackets, but that their calculations and results were based on the correct formula.

The Penn State/NCAR mesoscale model uses a staggered grid (Arakawa B). Consequently, velocities are stored at locations horizontally displaced from temperature and humidity. Interpolations of velocity are made to coincide to temperature locations before the Δ_{ij} differences in (1) are computed. Although this procedure is required for physical consistency with this particular host model, it unfortunately causes extra smoothing which can reduce the Δ_{ij} differences and alter the mixing potential.

Parameter values suggested by Stull and Driedonks are also used here: timescale $T_o = 1000$ s, critical Richardson number $R_c = 0.21$, and dissipation parameter $D = 1$. Along any row of the mixing-potential matrix, values closer to the main diagonal are increased if necessary to be no smaller than elements further from the diagonal to eliminate unrealistic convective overturning. The internal subgrid scale mixing potential, Y_{ii}, is then set equal to the largest element on its same row, plus a reference potential $Y_{ref} = 1000$. The net result is that we have used 4 parameters (T_o, R_c, D, and Y_{ref}) to parameterize a mixing-potential matrix with 15 x 15 unknowns.

At this point, the unequally-vertically-spaced grid points in the host model require a modification of the original equations suggested by Stull and Driedonks. A row-norm (RN_i) for each row in the transilient matrix is defined by the weighted sum of the mixing potentials:

$$RN_i = \sum_{j=1}^{n} m_j \, Y_{ij} \tag{2}$$

where m_j is the mass of air within grid layer j. Alternately, one can use the relative mass (or $\Delta\sigma$ within a sigma-coordinate model such as the Penn State/NCAR model) in place of m_j. The so-called L_∞ norm (i.e., the value of the one maximum row) is defined as a matrix-norm $\|Y\|_\infty$, as in Stull and Driedonks:

$$\| Y \|_\infty = \max_i \; (RN_i) \tag{3}$$

The off-diagonal transilient coefficients are parameterized by:

$$c_{ij} = \frac{m_j \, Y_{ij}}{\| Y \|_\infty} \tag{4a}$$

and the elements on the main diagonal are given by:

$$c_{ii} = 1 - \sum_{\substack{j=1 \\ j \neq i}}^{n} c_{ij} \tag{4b}$$

It is important to note that $c_{ij} \neq c_{ji}$, even if $Y_{ij} = Y_{ji}$, because $m_i \neq m_j$. Thus, Y_{ij} is symmetric, while c_{ij} is asymmetric. Furthermore, each row of the transilient matrix sums to one, but each column does not. In spite of this, total air mass and state variables are still conserved during the mixing process, and the mixing is assumed to represent an equal (but not necessarily total) exchange of mass between the grid points i and j. The above scheme works well with any arbitrary grid spacing, including the sigma coordinates of the host model. A more detailed explanation, derivations of the above equations, and examples of transilient matrices for unequally-spaced grid points are given in Appendix A.

Equations (2)-(4) above are exact expressions, based on conservation of mass; however, (1) is a parameterization that is only an approximation to nature. Recently, Stull (1989) compared the parameterized matrices with the matrices observed by Ebert et al. (1989), and found a systematic bias in (1). The parameterized matrices tend to cause erroneously large amounts of mixing at the bottom of each turbulent domain, compared to the mixing between grid points elsewhere within the domain, even for equally-spaced grid points. A similar conclusion was discovered earlier by Chrobok (1988) based on boundary-layer forecasts made with (1). For this reason, we designed a weighting scheme to counteract the unrealistic height-dependent mixing. For simplicity, we divided (4a) by m_j, which works for the Penn State/NCAR model only because the grid layer thickness increases monotonically with height. The net effect is to reduce the mixing into lower-altitude grid layers while increasing it in the upper layers. Although this correction scheme was used here as a quick fix, a better approach would have been to refine (1) into a more physically-realistic parameterization.

During any one timestep, the operations of equations (1) - (4) described above can be applied to one column at a time, until the whole domain of the host model has been turbulently adjusted. Occassionally we have stored the transilient matrix for each column for post analysis of turbulence characteristics; however, storage limitations on the computer precluded extensive use of this approach. Instead, we usually stored only yes/no information on the turbulence state of each grid point. These vertical cross sections of turbulence state are useful to highlight the boundary layer, frontal zones, and clear-air turbulence patches. Horizontal cross-sections show unstable air masses and frontal zones. Also, this information of turbulent subdomains is important input to the horizontal mixing scheme described in the next subsection. As a compromise between the storage of full turbulence details and limited computer storage, we sometimes save only the c_{ii} value for each grid point i, because it not only indicates if the point was turbulent ($c_{ii} < 1.0$), but the amount of mixing is indicated by the magnitude of $1.0 - c_{ii}$.

Next, step (iii) is accomplished with simple matrix multiplication applied to each of the mean field state variables in a column:

$$S_i\,(t+\Delta t) \;=\; \sum_{j=1}^{n} c_{ij}\,(t,\,\Delta t)\;\; S_j'(t\,) \tag{5}$$

Steps (ii) and (iii) are applied together, one column at a time.

d. Horizontal mixing

For step (iv), we explicitly assume that turbulence is a three-dimensional phenomenon. If there is (resolved) turbulent mixing in the vertical, then there is also mixing by the same (unresolved) eddies in the horizontal. If no turbulence has been found in a portion of a column based on the parameterizations of the previous subsection, then we assume that horizontal mixing cannot occur their either. For each height, we assume that horizontal mixing between two neighboring columns occurs only if both columns have turbulence at that height (see Fig 3). Also, we are not concerned with non-neighboring columns, because the column width is so large (80 km) and the timestep of the host model is so small (120 s) that turbulence can not physically mix beyond its neighbor during one timestep. This horizontal mixing between neighbors at first glance looks similar to K-theory, except that here we allow horizontal mixing only between neighbors that are turbulent.

The procedure is to examine each column one at a time. Define the column of interest by subscript i = 0, and each of its (up to) four neighbors on the same sigma surface by subscript i = 1 to 4. For each column, we then examine each height one at at time. Based on the existence of turbulence and the vertical size of the contiguous turbulent domain, we define horizontal mixing potentials $¥_{0i}$ at that one height.

We assume the horizontal mixing potential is equal to the fraction of a grid box width into which turbulence can transport state variables from a neighboring box. Using simple eddy-size arguments, this fraction is proportional to the lateral distance (h_{io}) that turbulence can mix during one eddy-cycle, times the number of eddy-cycles ($\Delta t/\tau$) that occur during one timestep, divided by the horizontal size of the grid box, Δx:

$$\yen_{oi} = \frac{h_{oi}\ \Delta t}{\Delta x\ \tau} \tag{6}$$

In this parameterization, we have assumed for computational efficiency that turbulent eddies are isotropic, and that the lateral mixing distance is proportional to the size of the largest eddies, which in turn is the vertical size (h_{io}) of the contiguous regions of turbulence that are simultaneously present in the neighboring columns. The effective timescale for one eddy cycle, τ, is unknown, and is treated as a parameter to be tuned during trial forecasts. We found $\tau = 100$ s to work best, given the NCAR/PSU timestep of 120 s. The subgrid-scale mixing potential ($\yen_{oo}$) is defined by (6), with h_{io} replaced by the total vertical domain of the host model. Furthermore, $\yen_{oi} = 0$ at any height if either the center column (o) or its neighboring column (i) is not turbulent at that height.

Step (v) can now be performed at each grid point within each column by applying the L_1 norm [shown in the denominator of (7)]:

$$S_o(\text{after horizontal mixing}) = \frac{\sum_{i=0}^{4} \yen_{oi}\ S_i\ (\text{before horiz. mixing})}{\sum_{i=0}^{4} \yen_{oi}} \tag{7}$$

The results of horizontal mixing are stored in a separate array until the computations have been completed for the whole domain. Thus the mixing potentials at a specified grid point, as determined by applying (6) and (7), are based on a 5-point stencil (see Fig 4). As a side note, (7) can theoretically be put in matrix form, and combined with (5) to yield one equation that can be inverted to yield a different *c* matrix that accomplishes both the vertical and horizontal mixing.

Some initial forecast tests were made with no horizontal mixing. In general, the solutions were numerically stable (both with and without the filter described in section 4); however, frontal boundaries became too sharp as the forecast progressed. When horizontal mixing was added, the frontal zones became more realistic. Also, horizontal mixing alters the temperature and wind profiles in some of the columns, which in turn alters the dynamic stability and vertical mixing. The combined nonlocal vertical and horizontal mixing are very strongly interdependent. The result is a quasi-3-D turbulence scheme that automatically forecasts boundary-layer evolution and patchy clear air turbulence.

e. Computational efficiency

We now examine the number of calculations involved in the turbulence parameterization during any one time step for a grid with N x M horizontal and L vertical discrete points.

The staggering of the grid in the Penn State/NCAR model (Arakawa B grid) requires that some interpolation be done in the calculation of the mixing or transilient coefficients in both the vertical and horizontal turbulence schemes. Specifically, the horizontal velocities are linearly interpolated to temperature grid point locations. These interpolated values are then used in the calculation of the mixing potential for the temperature and mixing ratio. The transilient coefficients associated with the temperature and mixing ratio fields are then retained and linearly interpolated to the staggered grid locations to give the transilient coefficients associated with the horizontal wind. Horizontal boundaries are assigned no-mixing potentials. Because of the staggered grid many extra calculations are required.

Bookkeeping processes require 147 NML arithmetic operations; i.e., operations requiring addition, subtraction, division or multiplication of a real or integer quantity. Determination of the mixing potentials for use in (5) can require between 189 and 250 NML operations depending on the amount of turbulence. Matrix multiplication requires 120 NML evaluations. All total, the greatest possible number of calculations required for an application of (5) to the entire domain is 517 NML operations not counting a maximum of 9 NML determination of a maximum value. If every point is turbulent the horizontal mixing formulation requires 179 NML operations. This give somewhere in the neighborhood of 700 NML, or less, arithmetic operations for the combined vertical and horizontal turbulence calculations. This is a substantial number of arithmetic operations, requiring more than a three-fold increase in the total computing time to make a 72 hr forecast, provided the turbulence parameterization is applied at every time step.

We will show in Section 5 that the transilient turbulence parameterization can increase the magnitude of the omega field by a factor of two, and therefore models severe-storm precipitation events better. It is well known that the magnitude of the vertical velocity is dependent on the grid resolution. Thus, we would expected similar behavior without TT if the grid resolution was enhanced by a factor of two or more. If this was done, small scale horizontal structures would be better represented and the omega field would benefit since the horizontal divergence is scale dependent. Doubling of the grid resolution, however, would cause an eight-fold increase in computing time. When measured against this increase, the transilient 3-fold increase provides an economic alternative.

A significant reduction (about one-fifth) in the total number of required calculations could be obtained if the grid was not staggered. Likewise improved vectorization would help but the parameterization is strongly centered around the vertical dimension, which being the smallest, limits the potential for improvement. We are optimistic that future research will find ways to significantly reduce the computational expense. However, the final authority that determines whether the parameterization is worth the expense is the quality of the forecasts.

3. Surface heat flux with molecular effects included

One of the major roles of turbulence is to transport heat and moisture from the surface to the rest of the atmosphere. Turbulence cannot accomplish its task until molecular processes have first transported the heat and moisture from the nonturbulent surface into the lowest few millimeters of air. Thus, transport from the ground to the air is controlled by both molecular and surface-layer physics.

Flux-profile relationships for the surface layer empirically describe only the turbulent contribution to flux. Given measurements of potential temperature difference between two heights within the turbulent surface layer, for example, a heat flux can be estimated. It is physically inappropriate to use a temperature difference between the ground/sea surface and the air in such a surface-layer parameterization. We show below how surface layer and molecular layer parameterizations can be combined to estimate flux from the ground-to-air temperature difference.

The heat flux used in the surface-layer turbulence calculations within the Penn State/NCAR model is computed from similarity theory (Businger et al., 1971):

$$H_s = -\rho C_p k u_* T_* , \qquad (8)$$

where T_* is given by

$$T_* = (\theta - \theta_s) / (\ln(z_a/z_o) - \psi_H) . \qquad (9)$$

The parameter ρ is the density, k is the von Karman constant of 0.4, C_p is the specific heat of air at constant pressure, θ_s is the potential temperature at a nominal "surface" height z_s while θ_a is the air potential temperature at the lowest model level z_a. The friction velocity, u_*, is expressed as

$$u_* = \mathrm{Max}[\, u_{*o} ,\ k V / (\ln(z_a/z_o) - \psi_M) \,] , \qquad (10)$$

where $u_{*o} = 0.1\ \mathrm{ms}^{-1}$ and $V = (V_a^2 + V_c^2)^{0.5}$. Here V_a is the wind speed at height z_a and V_c is a convective velocity (Anthes et al., 1987). The roughness height is z_o. The nondimensional stability parameters ψ_H and ψ_M are a function of the bulk Richardson number (Anthes et al., 1987).

Combining (8) thru (10) yields

$$H_s = -c_1 (\theta_a - \theta_s) , \qquad (11)$$

The original parameterization erroneously uses the ground skin or sea-surface temperature for θ_S, which violates the assumptions of the similarity theory. Instead, we will assume that θ_S is the temperature in the air at the bottom of the turbulent surface layer, which corresponds with the height z_μ of the top of the nonturbulent viscous microlayer (Stull, 1988).

In the molecular layer, the molecular heat flux at z_μ is given by the diffusion equation:

$$H_{s\mu} = -\rho K_{H\mu} (T_s - T_g) / z_\mu \equiv -c_2(\theta_s - \theta_g). \qquad (12)$$

Here $K_{H\mu}$ is the molecular conductivity in air, and θ_g is the surface-skin temperature.

By matching the heat fluxes ($H \equiv H_s = H_{s\mu}$) and θ_S between the surface layer and microlayer, we can combine (11) and (12) to yield:

$$H = -c_1 (\theta_a - \theta_g) (1+ c_1/c_2)^{-1} \qquad (13a)$$

or

$$H \equiv -c_1 c_3 (\theta_a - \theta_g) \qquad (13b)$$

where

$$c_3 \equiv (1+ c_1/c_2)^{-1} . \qquad (14a)$$

and

$$c_1/c_2 \cong c_p k^2 V z_\mu /[K_{H\mu} \ln(z_a/z_o - \psi_M) \ln(z_a/z_o - \psi_H)] \qquad (14b)$$

We see that (13b) is similar to (11), except that the additional factor c_3 appears when the ground skin temperature is used in place of a surface air temperature. For typical values of V, z_a, z_μ, and z_o (e.g., $V = 5\ ms^{-1}$, $z_a = 50$ m, $z_\mu = 0.01$ m and z_o between 0.01 and 0.5), we obtain for c_3 a range of values between 0.20 and 0.06. Consequently it is clear that the molecular layer reduces the heat flux in (13b) by at least 80% for any given temperature difference.

Over land surfaces, however, the ground skin temperature is not fixed, but responds to the surface energy balance. Thus, a fixed rate of insolation will cause the ground skin temperature to become warmer than in the original Penn State/NCAR model, resulting in a new equilibrium heat flux that is nearly the same magnitude as in the original model (i.e., it will be 5 - 10% less, rather than 80% less). Although there is little net change in heat flux, the ground temperature is now significantly warmer/cooler than the air temperature during day/night, and there is a strong temperature gradient across the microlayer. In our model runs we have tested forecasts where the value of c_3 is fixed at 0.2, 0.1 or allowed to vary over a fixed range ($0.1 < c_3 < 0.2$). For all cases we found (13b) to be a more realistic and consistent parameterization for the heat flux at the surface than the original parameterization.

The original surface moisture flux, E, parameterization in the Penn State/NCAR model was similarly modified to include the c_3 parameter associated with the viscous microlayer over land:

$$E = -c_1 c_3 \frac{M_a}{C_p} (q_a - q_g) \qquad (15)$$

where M_a is the moisture availability parameter, q_a is the specific humidity at the lowest grid point in the air, and the ground moisture q_g is taken as the saturation specific humidity at the ground skin temperature.

4. The Implicit Tangent Filter

Numerical forecast models normally require dissipative finite difference schemes or artificially enhanced viscosity to maintain numerical stability. The Penn State/NCAR regional model is known to become unstable when the horizontal diffusion is reduced below a critical value (Errico and Baumhefner, 1987). In contrast, we find the TT version of the model to be numerically stable, for the cases considered, when we removed all K- theory diffusion. This is true with or without the horizontal mixing component in the turbulence parameterization. Stull (1986) had proved that TT by itself is numerically stable; however, we were surprised to learn that the host model remained stable, in spite of the patchy sporadic turbulence produced by TT.

Nevertheless, the sporadic nature of the forecasted upper-level turbulence, and the growth and decay in the boundary layer did introduce light to moderate amounts of numerical noise in the horizontal directions. Even though the magnitudes of these features remained finite in time it is still desirable to remove all scales that cannot be represented accurately by the finite difference scheme. Filters are commonly used in numerical models to remove high frequency noise that can not be resolved. Among the most familiar are the Shapiro (1970,1975) and Shuman (1957) filters. In this study we apply the sixth order low-pass implicit tangent filter (Raymond, 1988). This filter possesses some very desirable characteristics, viz., it has an extremely sharp roll-off in the amplitude response function, can be applied near horizontal boundaries and it contains a filter parameter ε (equation in APPENDIX B) which can be adjusted to give the desired smoothing.

The implicit calculations require the inversion of a banded diagonally dominant matrix. For order two, the filter studied in Pepper, et al., (1979) is recovered. As the order is increased the roll-off in the amplitude response is greatly sharpened. The characteristics of the sixth-order low-pass implicit tangent filter are best illustrated by examining the amplitude response function given in Appendix B. This response is similar to that given by the recursive tangent filters described in Otnes and Enochson (1978). However the implicit tangent filter is nevertheless much easier to work with because the coefficient weights are known and boundary conditions encountered in limited area modelling are easily handled in the implicit formulation.

In Fig. 5 the response of the filter is shown after 24 hrs (720 applications with ε=0.0075) and is compared with the 4th order K theory horizontal smoothing normally used in the Penn State/NCAR regional model. Note for wave number $6\Delta x$ that the responses are much closer to the unfiltered value of 1 when using the 6th order implicit filter, whereas the 4th order K theory operator removes almost all of these features, especially when the maximum K value is used. The filter, with ε=.0075, is applied at every time step in the model to the horizontal wind velocity components, the temperature and the mixing ratio fields. The filter parameter ε was selected to give the lowest acceptable smoothing while still maintaining reasonable smooth fields. The application of the filter takes place after completion of the new time step and following the turbulence parameterization.

5. Discussion of Results

a. The OSCAR IV case

The percent of the total number of horizontal grid points that contain turbulent exchanges, for the OSCAR IV case, is illustrated in Fig. 6 as a function of pressure and time, as predicted from a 72 hr forecast with the TT parameterization. Note that above the 500 mb level approximately one percent or less of the total number of the horizontal grid points are turbulent. The maximum at high levels occurs during the strongest cyclonic intensification which takes place between hours 18 through 48. In the lowest levels of the boundary layer, more than 75% of the total horizontal grid points are turbulent during the peak heating in the diurnal cycle. Clearly there is a significant diurnal variation within the boundary layer.

The horizontal distribution of turbulence in the boundary layer is shown in Figs. 7a,b. In Fig. 7a the distribution of the turbulence 21 hours into the forecast (near 3 pm local time) at σ=0.94 corresponds closely with the heated land mass. Only in the midwest (associated with the major cyclonic activity) is there a turbulence-free zone. This most likely occurs because of the stabilizing radiative and evaporative properties associated with the precipitating clouds. Also note the lack of turbulence over the water surface. At higher levels in the atmosphere (σ=.74) the turbulence is confined to the mountainous regions as shown in Fig. 7b .

Vertical cross sections through the center of our region (taken west to east) are presented in Figs. 8a,b showing the potential temperature θ (K) and the mixing ratio
(g kg^{-1}). Regions with turbulence are within or under the wide solid line found in the θ field in Fig. 8a. The turbulent (mixed) boundary layer appears deepest over the mountains and just ahead of the front as shown between grid points 30 and 45, which is very realistic. Some turbulence is also occurring at mid-levels within the frontal zone above grid points 29 and 30. Note that some folding in the θ contours occur at mid levels between grid points 25 and 35 indicating the presence of the cold

front. Clearly the largest amount of moisture is found in the warm sector. This is reflected in the contours of mixing ratio in Fig. 8b which have their greatest vertical extent between grid points 30 and 45.

There is some likelihood for the fluid near and parallel to the front to behave quasi-two dimensional. It is well known that two-dimensional turbulence cascades energy toward the larger scale (Kraichnan and Montgomery, 1980). To retain the true character of the flow, three dimensional turbulence is necessary. In our study we have found that the horizontal variation of meteorological fields in the vicinity of the cold front are very dependent on the horizontal mixing (7). In Figs. 9a and 9b we show the mixing ratio field for the lowest sigma level, 48 hrs into the forecast, for simulations made with and without the horizontal turbulence. Without the horizontal mixing the gradients become too large and unrealistic (Fig. 9b). In our three dimensional TT formulation we found that $\tau=100$ in (6) gave reasonable results. The results in Fig. 9b are seen to compare reasonably well with the control Blackadar simulation shown in Fig. 9c. Increasing the horizontal mixing by reducing the value of τ even more would appear beneficial.

The rms error at 850 mb in the forecast temperature is shown in Fig. 10. Results from four forecasts are displayed. The control run is the Penn State/NCAR model with the existing Blackadar boundary layer scheme and K theory horizontal diffusion. The control was run with a Kuo cumulus parameterization and with an explicit cloud scheme, labeled (clouds) in Fig. 10 (Hsie and Anthes, 1984). In the explicit cloud scheme prognostic equations are included for cloud water and rain water. Also, evaporation of cloud and rain water in unsaturated layers are part of the process but the ice phase is not considered in our calculations. In the TT parameterization version we run identical simulations except no cumulus parameterization was utilized in any of our numerical forecasts. Note in Fig. 10 that the rms errors, determined when forecast and radiosonde values are compared, are least for the transilient approach with explicit clouds, except near the end of the 72 hr forecast. Overall, carrying the clouds explicitly made little difference in these rms statistics, but we found that feedback processes, e.g., cloud and rainwater evaporation, are of the utmost importance. Evaporation is included when the clouds are explicitly carried; otherwise, the current version of the Penn State/NCAR region model does not include this process. Zhang et al. (1988) have shown that including realistic physics, e.g., evaporation and water loading, reduces model tendencies for over development. In this study of a new turbulence parameterization cloud and rain water are not directly included in the turbulent mixing. That topic is left for future consideration.

The effect of explicit clouds is however very clear in the mean error in the 850 mb temperatures shown in Fig. 11. Note that a change in sign is associated with whether the clouds are carried explicitly. The TT scheme gave nearly zero mean error at hours 12 and 24 , and has the smallest mean error of the four forecasts. The control run, with and without explicit clouds, generally has much larger mean errors.

In Fig. 12 the mean sea-level pressure 48 hrs into the forecast is shown for the control runs, Kuo cumulus parameterization (Fig. 12a), explicit cloud (Fig. 12b), and for the TT version with explicit cloud (Fig. 12c) and for the verification analysis (Fig. 12d). Note that the low pressure centered over the great lakes is best represented in the TT forecast which has the correct pressure of 997 mbs but over a reduced area as compared to the verifying analysis in Fig. 12d. The contraction of the surface low in the TT case is similar to the control case, with explicit cloud calculations, which has a central pressure of 996 mb. The control with the Kuo scheme has a 990 central pressure, so the low is deepened too much. As a consequence of this the 1008 pressure contour is however in a location closer to that indicated in the verifying analysis. Otherwise over most of the remaining area the control cases are slightly better by a small margin, but the presence of topography is a complicating factor making interpretation difficult.

To gain some idea of the response at the surface we now turn our attention to Figs. 13a and 13b showing the surface slab or skin temperature, 48 hrs into the forecast at 0000 UTC 24 April, for the control case with explicit cloud calculations and the equivalent transilient turbulence simulation (c_3 fixed at 0.2). A comparison of these two figures shows that they are nearly the same in the north-eastern portion of our region while in the western part the skin temperature differences are up to 4 degrees in some locations. We expected and wanted slightly warmer surface skin temperatures in the transilient version. Remembering that the fluxes are being reduced by c_3 in (13b), which compensates for the molecular layer, means that the overall heat flux felt by the lowest layer should be the same order of magnitude as that observed in the control case.

Rainfall is strongly correlated with convective activity and the vertical velocity. One useful gauge to measure development is the omega L_2 norm, i.e.,

$$\omega_{norm} = [\ \Sigma\Sigma\Sigma\ \omega^2_{ijk}/\#]^{1/2}, \tag{16}$$

where # is the total number of grid points in the volume. The variation of the omega norm with time for the OSCAR IV case is shown in Fig. 14. The conversion is that 10^{-3} Pa s^{-1}= 36 mbs hr^{-1}. The control or Blackadar scheme shows little variation with time while the TT scheme exhibits significant changes, i.e., note the increase during the second day and the diurnal variation of the omega norm. A maximum is found during the afternoon hours and again at night, (forecast hours 0, 24, 48 and 72 correspond to 000 UTC). Allowing c_3 to vary ($0.1 < c_3 < 0.2$, labeled Var in legend) reduces the norm while the introduction of the explicit cloud calculations, including evaporation, also reduces the magnitude especially after hour 40. Therefore details in the surface flux and viscous layer calculations can make a significant difference in the forecast. In spite of the enhanced vertical motions rainfall is only slightly heavier (bias score increased by 25% for threshold > 2.64 cm.) with the transilient turbulence parameterization.

The cumulative rain and evaporation for the 72 hr forecast is shown in Fig. 15. The explicit cloud simulations are labeled 'Exp' while 'Reg' refers to only large scale rainfall except in the control where the Kuo cumulus parameterization scheme is also included. Note that in the TT forecasts the rainfall is excessive without the feedback mechanisms of evaporation and water loading. Allowing c_3 to vary, labeled Var, also reduces the total precipitation. However the largest difference between the control and the new TT parameterization is found in the cumulative evaporation columns. This difference is primarily due to the inclusion of the viscous layer in the moisture flux calculations (15). Evapotranspiration processes have not been included in any of our simulations.

b. The CAPTEX case

The omega norm for the CAPTEX case is illustrated in Fig. 16. The control version exhibits only a flat curve, while using the TT parameterization ($c_3 = 0.2$) gives a large diurnal variation which peaks during the early night (forecast hours 12, 36 and 60 correspond to 0000 UTC). It is very characteristic of mesoscale convective systems to exhibit a nocturnal maximum in precipitation (Kane et al., 1987). This diurnal variability has also been noted in tropical regions by Gray and Jacobson (1977) and Meisner and Arkin (1987). As in the OSCAR IV case the inclusion of explicit clouds makes a significant difference. Explicit clouds with cloud and rain water evaporation processes included keep the three diurnal peaks at about the same intensity, while the maximum grows in time when evaporation processes are not considered. These findings help substantiate the conclusion reached by Zhang et al. (1988), .i.e., that feedback processes are important to keep the numerical models from developing run-away convection. We now examine this and other feedback processes in greater depth.

It have been known for some time that many processes, e.g., radiation and cloud and rain water evaporation, are important and should be included to realistically model the earth's atmosphere. But when these processes are included in some traditional numerical models the response signal is only faintly discernible or is hard to interpret. We now examine the role of feedback mechanisms utilizing our newly created TT model with the CAPTEX initial and boundary data sets. Comparisons are also made with the control version. A complete description of the feedback processes utilized in the Penn State/NCAR region model is found in Anthes et al (1987). Additional sources for details on the physics include; Hsie et al. (1984) for a description of the evaporative processes, Zhang and Anthes (1982) present details about the surface budget calculations and Benjamin and Carlson (1986) outline the long and short wave radiation calculations. In Fig. 17a we see that when cloud and rain water evaporation is removed from the transilient turbulence explicit cloud calculations (TT No Cloud Evap) the omega norm is substantially increased in magnitude as compared to the transilient forecast with that process included (TT). With the removal of evaporation in the air convection has becomes much more pronounced so a major part of the diurnal variation is no longer present. Likewise we see that removing the atmospheric component of the radiation (TT No Atm Rad) enhances the omega norm as does the removal of radiative cloud feedback to the surface radiation budget (TT No Cloud Rad). Thus, all these feedback reactions help control the degree of convection. It is thus clear from our numerical results that the feedback processes examined here are very important to our 72 hr forecast.

The same four physical feedback tests, also for explicit cloud calculations, are computed for the control version of the model. The omega norm for each is shown in Fig. 17b. Evaporation has a strong signal predominantly during the latter half of the forecast. The effect of the other two physics mechanisms are more difficult to interpret since after 72 hrs both omega norms are less in magnitude than the full physics case (heavy solid line). Not only is the shape of the curves different but the response and the timing of the response is also clearly different than that shown in Fig. 17a.

We postulate that the feedback or physics processes become more important as the numerical model become better able to simulate the atmosphere. The fact that different responses are clearly visible in Fig. 17a within just twelve hours into the forecast implies that numerical weather prediction and climate models can not ignore these (and other) processes and expect to simulate the atmosphere successfully. In fact, with the TT parameterization we found that the model returns a coherent signal in the omega norm (not shown) when the net radiative flux is changed by just one percent. Even though this signal is very faint it is still detectable within twelve hours in the difference field between the forecasted omega norms computed with 100% and 99% of the net radiative flux.

We now examine one of the most difficult processes to simulate correctly, i.e., precipitation. The change in the total area hourly precipitation, a measure of the precipitation rate, is shown in Fig. 18 for the TT procedure (heavy line) and for the convective and large scale values associated with the control or standard Penn State/NCAR model. Notice the diurnal variation in the TT forecasted precipitation. Peak values occur during the early night time hours but some small oscillations occur during early afternoon maximum surface heating periods. As expected the precipitation and omega norm have very similar behavior as seen by comparing Figs. 16 and 18. In contrast, in the control simulations the Kuo convection scheme peaks at maximum surface heating times during the first half of the forecast period (Fig. 18). The following 36 hrs is a period of predominantly increasing precipitation. The large scale rainfall (control) shows little variation but a gradual increase peaks 31 hrs into the forecast.

The question remains: are there observations verifying the diurnal early night time peaks predicted using TT? To assist with answering this question we examine satellite visible and IR images. Four separate time periods are shown in Fig. 19. Note how the convective cloud activity increases and then decays over the time period 2100, 0000, 0300 and at 0600 UTC for the 25th and 26th of September 1983. The maximum convective activity occurs somewhere between between hours 0000 and 0300 UTC. Clearly, upward vertical motion should be associated with these centers of development.

The omega field predicted in the TT forecasts are radically different from that given by the control. The magnitudes and scale of the vertical motion is clearly different as revealed in Figs. 20a and 20b, representing the horizontal slice for the 8th sigma level (approximately 766 mb standard atmospheric pressure level) for the TT and the control 36 hr forecasts, respectively. Note how with TT (Fig. 20a) there are rolls in the right center of the figure whose slope parallels the U. S. East Coast and the Appalachian Mountains. These feature are absent in the control. Comparing the region of dashed lines or negative omega values, in Fig. 20a with the cloud cover in Fig. 19 gives a good correlation. Clearly the magnitudes of these updrafts are much larger than those in Fig. 20b. The placement of the updrafts in TT coincides very well with the rainfall pattern particularly in Mexico and in the Colorado Rockies, but the rainfall amounts associated with some of the more intense updrafts, are much too heavy.

The accumulated rainfall as a function of time is shown in Fig. 21. Note that the totals for the TT approach and the control, with Kuo cumulus parameterization, are nearly the same. The diurnal oscillation is apparent in the TT results. In the control forecast the convective rainfall is larger than the large-scale nonconvective component. Because the TT approach parameterizes the mixing in the vertical from unresolved horizontal scales we do not find it necessary to include cumulus parameterization.

The variation of the total cumulative rainfall and evaporation for five different 72 hr forecasts is shown in Fig. 22. The TT forecasts are labeled TT and those from the control are labeled with Blackadar. Both explicit cloud calculations (Exp) and the regular (Reg), which includes the Kuo cumulus parameterization for the control only, are presented. Note the significant reduction in total rainfall for the explicit cloud cases. Removing the horizontal mixing in the turbulence calculations (7a), labeled No Horiz, increases the rainfall. Also obvious in Fig. 22 is the significant differences in the recorded amount of evaporation derived from the surface.

The heat flux for the 72 hr forecast period computed at point (x_{25},y_{25}) is shown in Fig. 23a. (The numbering of the grid begins at the lower left hand corner.) Values computed from (13) and (14), and those computed in the control, are shown. The control surface flux is larger in magnitude but the pattern is very distorted at the lowest atmospheric level (HFLUX 15) during the first twelve hours of the forecast, in contrast to that given by the more physically realistic approached use in this study. Likewise the moisture-flux patterns (Fig. 23b) are very similarly behaved. In Fig. 23b we see that the control shows some tendency for an enhancement of the moisture flux with time in contrast to nearly cyclic behavior in the TT model calculations. The large fluctuation seen with the control are absent in our TT results.

The bias in the rainfall, measuring the tendency of the model to forecast too small (<1) or too large (>1) an area of precipitation for a 72 hour forecasts, is illustrated in Fig. 24. Including the clouds and evaporation in the TT cases reduces the over-estimation for the heavier rainfall but does affect the light rain cases because of the water loading by the clouds. Otherwise the TT parameterization with explicit clouds, even with the much larger omega norm, gives accurate results with respect to the placement of the precipitation, but the amounts of precipitation is sometimes overestimated in local areas by a factor of two or three.

This accuracy is also revealed in the 850 mb geopotential heights. The rms error with respect to radiosonde measurements is shown in Fig. 25a. The forecasts utilizing the transilient turbulence parameterization are clearly superior, i.e., the rms error is reduced by more than a third. The mean error is likewise significantly reduced using the TT scheme as indicated in Fig. 25b.

6. Conclusions

The first-order non-local turbulence parameterization known as transilient turbulence (TT) has been incorporated into the Penn State/NCAR 15 sigma level regional primitive equation mesoscale model. This required that the host model be modified by removing the existing representations for the horizontal and vertical K-theory eddy diffusion and the dry and moist convective adjustment routines. In their place we substitute the unified approach described by the TT parameterization. Additionally, a sixth order implicit tangent filter was inserted to remove numerical noise, thus separating computational considerations from the physical turbulence parameterization. In the surface heat and moisture flux calculations a new procedure incorporating a molecular viscous layer was used to improve the surface physics. Together, the changes espoused here represent a major departure from the traditional modelling norm, as represented by the host model. To test the TT parameterization we made 72 hr forecasts using the OSCAR IV and CAPTEX initial and boundary data sets.

In TT the parameterization is based, in this study, on the turbulent kinetic energy equation. The vertical component in the TT scheme is applied first and turbulent grid points are identified. A horizontal mixing scheme is then applied only between neighboring grid points that were turbulent in the vertical. Both schemes together comprise the three dimensional TT procedure. The calculations of vertical mixing within the unevenly-spaced sigma coordinate grids were modified, as described in Section 2, from the conceptual formulation described in Appendix A. The gauge used to measure the desired amount of mixing was precipitation. We found in both the OSCAR IV and CAPTEX cases that the amount and nature of the vertical mixing had a direct bearing on the amount and location of the precipitation. The modifications described in Section 2 yielded satisfactory results for our vertical grid configuration. Additional improvements are still possible. Nevertheless the current results from two case are very promising and show that major modelling improvements can result. Additional case studies are being used.

The three dimensional TT parameterization scheme was found to be numerically stable, to accurately portray boundary layer characteristics, and to greatly improve the forecast accuracy for the CAPTEX case. By far the largest amount of turbulence occurred in the boundary layer. The new surface heat flux calculations, which includes a viscous layer, improved the communication between the earth's surface and the surrounding boundary layer. This enabled the TT scheme to build the well-mixed boundary layer. During the morning and early afternoon the boundary layer grew because of the surface heating. Thus the number of grid points experiencing turbulence reflects the diurnal cycle.

The omega norm, and hence the omega fields themselves, also experience a diurnal variation, but now the maximum occurs during the early night time hours. We believe the magnitude of this change to be too large but the placement of the updrafts coincide nicely with precipitation verification. The forecasted precipitation maximums also coincide with the nocturnal omega maximum. These nocturnal precipitation maximums are common to land-based mesoscale convective systems, so the turbulence forecasts are thought to simulate the atmosphere correctly. Satellite IR images verify our forecasts by showing enhanced convective cloud cover during early night time hours.

Because of the large variation of the omega field in time, and because of the larger omega magnitudes, the TT model is much more sensitive to how physical quantities are represented. For example, evaporative cooling now becomes extremely important. Explicitly including clouds, even for the 80 km horizontal grid considered here, becomes important because the evaporative processes are only included in that portion of the model code. Atmospheric radiation and cloud radiation feedback processes that influence the surface calculations are also shown to be significant. Boundary-layer parameters and calculation details were also found to be important. We suspect that additional physical processes like the role of evapotranspiration, cirrus clouds and cloud micro-physics may now play a much larger role in the model with the turbulence parameterization than in the control version.

Even though there are significant reductions of error in the boundary layer calculations and improvements in precipitation prediction in predominantly the CAPTEX case, statistically there remains little difference between the control and the TT forecasts at 500 mbs and above. However there are local differences primarily due to turbulence in the vicinity of jets, but for the geopotential heights at 500 mbs the overall forecasts have nearly identical rms error statistics, as determined from radiosonde reports. This is true for both the OSCAR IV and CAPTEX cases.

In the Penn State/NCAR regional model the computational time required for the transilient turbulence calculations is more than three times that required with the Blackadar or control version of the model. However, with the new turbulence parameterization the magnitudes in the forecasted omega fields are more than double that given by the control. Because the horizontal divergence is scale dependent we would expect similar behavior of the omega magnitudes if the grid resolution was increased by a factor of two. This latter calculation would however take about eight times that required by the course grid. Thus the transilient turbulence scheme represents a desirable alternative. Continued research and better model and algorithm development should reduce the computational expense. Clearly the computational overhead would be much less, in a relative sense, in numerical models which use a larger time step size, e.g., semi-implicit time integration or semi-Lagrangian procedures. The TT scheme is ideally suited for non-staggered grids thus the Arakawa A grid is the ideal. Staggered grids greatly enhance the computational expense and the necessary interpolations unduly modify the presence and concentration of the turbulence.

We have shown that the transilient turbulence parameterization improves the boundary layer behavior, predicts CAT and forecasts omega fields which exhibit a large diurnal variation with a nocturnal maximum. Forecast statistics are definitely improved for the CAPTEX case. We also found that physical feedback processes like atmospheric radiation, cloud radiative properties on the surface calculations and cloud and rainwater evaporation all give an important signal with a positive contribution to the 72 hr forecasts. These processes are shown to be all important in simulating the atmosphere accurately.

We believe that with the aid of additional refinements the transilient turbulence procedure has the potential to significantly improve numerical weather prediction.

Acknowledgements

The authors thank Richard Anthes and the NCAR personnel for sharing with us the Penn State/NCAR regional model and for providing the OSCAR IV and CAPTEX model and verification data sets. A special thanks goes to E. Hsie, S. Lownam and E. Donall for the help they provided. We also thank Gary Wade (National Environmental Satellite Data and Information Service, NOAA) for assisting with the satellite images. This work is supported by the National Science Foundation under grants ATM-8508759 and ATM-8517139, and by AFGL contract F19628-87-K-0035. One author (WHR) was also supported in part from CIMSS's contract NA84AA-H-00028. Computer resources were supplied by the National Center for Atmospheric Research, which is sponsored by the National Science Foundation.

7. References

Andre, J.-C., G. DeMoor, P. Lacarrere, G. Therry and R. du Vachet, 1987: Modeling the 24-hour evolution of the mean and turbulent structures of the planetary boundary layer. *J. Atmos. Sci.*, **35**, 1861-1883.

Anthes, R.A., 1983: Regional models of the atmosphere in middle latitudes. *Mon. Wea. Rev.*, **111**, 1306-1335.

Anthes, R. A., and T. T. Warner, 1978: Development of hydrodynamic models suitable for air pollution and other mesometeorological studies. *Mon. Wea. Rev.*, **106**, 1045-1078.

Anthes, R. A., E.-Y. Hsie, and Y.-H. Kuo, 1987: Description of the Penn State/NCAR Mesoscale model version 4 (MM4). NCAR technical note NCAR/TN-282+STR. 66 pp.

Benjamin, S. G., and T. N. Carlson, 1986: Some effects of surface heating and topography on regional severe storm environment. Part I: Three-dimensional simulations. *Mon. Wea. Rev.*, **114**, 307-329.

Berkowicz, R. and L/P. Prahm, 1979: Generalization of K-theory for turbulent diffusion. Part I. Spectral turbulent diffusivity concept. *J. Appl. Meteor.*, **18**, 266-272.

Boussinesq, J., 1877: Essai sur la theorie des eaux courantes. *Mem. pres. par div. savants a l'Academie Sci., Paris*, **23**, 1-680.

Businger, J.A., J.C. Wyngaard, Y. Izumi and E.F. Bradley, 1971: Flux profile relationships in the atmospheric surface layer. *J. Atmos. Sci.*, **28**, 181-189.

Chrobok, G., 1988: *Zur numerischen Simulation konvektiver Grenzschichten mit intergralen Schleißungsansätzen.* M.S. thesis (Diplomarbeit), Inst. für Meteorolgie und Klimatologie der Universität Hannover. 92pp. (Available from Stull, Univ. Wisconsin).

Ebert, E.E., U. Schumann, and R.B. Stull, 1989: Nonlocal turbulent mixing in the convective boundary layer evaluated from large-eddy simulation. *J. Atmos. Sci.*, (in press).

Errico, R., and D. Baumhefner, 1987: Predictability experiments using a high-resolution limited-area model. *Mon. Wea. Rev.*, **115**, 488-504.

Gray, W. M., and R. W. Jacobson, Jr., 1977: Diurnal variation of deep cumulus convection. *Mon. Wea. Rev.*, **102**, 1171-1188.

Heisenberg, W., 1948: On the theory of statistical and isotropic turbulence. *Proc. R. Soc. London, Ser.* , A **195**, 402-406.

Hsie, E.-Y., and R. A. Anthes, 1984: Simulations of frontogenesis in a moist atmosphere using alternative parameterizations of condensation and precipitation. *J. Atmos. Sci.*, **41**, 2701-2716.

Hsie, E.-Y., R. A. Anthes, and D. Keyser, 1984: Frontogenesis in a moist atmosphere. *J. Atmos. Sci.*, **41**, 2581-2594.

Kane, R. J. Jr., C. R. Chelius and J. M. Fritsch, 1987: Precipitation characteristics of mesoscale convection weather systems. *J. Climate Appl. Meteor.*, **26**, 1345-1357.

Kao, C. J., and T. Yamada, 1988: Use of the CAPTEX data for evaluation of a long-range transport numerical model with a four-dimensional data assimilation technique. *Mon. Wea. Rev.*, **116**, 293-306.

Kraichnan, R. H., and D. Montgomery, 1980: Two-dimensional turbulence. *Rep. Prog. Phys.*,**43**, 547-619.

Louis, J. F., 1979: A parametric model of vertical eddy fluxes in the atmosphere. *Bound.-Layer Meteor.*, **17**, 187-202.

Meisner, B. N., and P. A. Arkin, 1987: Spatial and annual variations in the diurnal cycle of large scale tropical convective cloudiness and precipitation. *Mon. Wea. Rev.*, **113**, 2009-2032.

Mellor, G. L., and T. Yamada, 1982: Development of a turbulence closure model for geophysical fluid problems. *Rev. of Geophy. and Space Phys.*, **20**, 851-875.

Otnes, R. K., and L. Enochson, 1978: *Applied Time Series Analysis, Volume 1, Basic Techniques.* John Wiley & Sons, New York, 449 pp.

Pepper, D. W., C. D. Kern and P. E. Long Jr., 1979: Modeling the dispersion of atmospheric pollution using cubic splines and chapeau functions. *Atmos. Envir.*, **13**, 223-237.

Prandtl, L., 1925: Bericht uber Untersuchingen zur ausgebildeten. *Turbulenz. Z. ang. Math. Mech.* **5**, 136-137.

Raymond, W. H., 1988: High-order low-pass implicit tangent filters for use in finite area calculations. *Mon. Wea. Rev.*, **116**, 2132-2141.

Shapiro, R., 1970: Smoothing, filters and boundary effects. *Rev. Geophys. Space Phys.*, **8**, 359-387.

Shapiro, R., 1975: Linear filtering. *Math Comput.*, **29**, 1094-1097.

Shuman, F. G., 1957: Numerical methods in weather prediction, II, Smoothing and filtering. *Mon. Wea. Rev.*, **85**, 357-361.

Stull, R. B., 1984: Transilient turbulence theory. Part I: The concept of eddy mixing across finite distances. *J. Atmos. Sci.*, **41**, 3351-3367.

Stull, R. B., 1986: Transilient turbulence theory. Part III: Bulk dispersion rate and numerical stability. *J. Atmos. Sci.*, **43**, 50-57.

Stull, R. B., 1987: Transilient turbulence algorithms to model mixing across finite distances. *Envir. Software*, **2**, 4-12.

Stull, R.B., 1988: *An Introduction to Boundary Layer Meteorology.* Kluwer Academic Publ. 666pp.

Stull, R.B., 1989: A comparison of measured vs. parameterized transilient matrices. (Submitted to *Bound.-Layer Meteor.*)

Stull, R. B. and A. G. M. Driedonks, 1987: Application of the transilient turbulence parameterization to atmospheric boundary layer simulations. *Bound.-Layer Meteor.*, **40**, 209-239.

Stull, R. B. and T. Hasegawa, 1984: Transilient turbulence theory. Part II: Turbulence adjustment. *J. Atmos. Sci.*, **41**, 3368-3379.

Stull, R. B. and E. Kraus, 1987: The transilient model of the upper ocean. *J. Geophy. Res.-Oceans*, **92**, 10745-10755.

Wyngaard, J. C. 1982: Boundary layer modeling. In *Atmospheric Turbulence and Air Pollution Modelling*. Eds. F. T. M. Nieuwstadt and H. van Dop, Reidel, Dordrecht, Holland, 69-1061.

Zeman, O., 1981: Progress in the modeling of planetary boundary layers. *An. Rev. Fluid Mech.*, **13**, 253-272.

Zhang, D., and R. A. Anthes, 1982: A high-resolution model of planetary boundary layer-Sensitivity tests and comparisons with SESAME-79 data. *J. Appl. Meteor.*, **21**, 1594-1609.

Zhang, D.-L, E.-Y Hsie, and M. W. Moncrieff, 1988: A comparison of explicit and implicit predictions of convective and stratiform precipitating weather systems with a meso-β-scale numerical model. *Q. J. R. Meteorol. Soc.*, **114,** 31-60.

Appendix A

Transilient Parameterization for Unequal Grid Spacing

a. A physical interpretation of nonlocal mixing

First, picture a column of 10 equally-spaced grid points as sketched in Fig A1a. Let each grid box be filled with one unit mass of air. Furthermore, assume for the sake of example that there is total ***exchange*** of only those units masses of air as sketched in Fig A1a. For example, all of the air from grid box *a* moves into box *d*, and all of the air originally in *d* moves to *a*, with similar interpretations for the other mixing arrows drawn. The transilient matrix for this case is symmetric, as shown in Fig A1b.

Next, group those unit boxes of air into larger grid boxes of different sizes (indexed as 1 to 4), as shown in Fig A1c, but assume the same mixing processes are occurring. The new grid box 1 is very small, and after mixing it holds precisely one unit mass that came from the new grid box 3; thus $c_{13} = 1.0$. Grid box 3 is larger, thus the unit mass of air that returned from box 1 accounts for only 33% of the final mass in box 3; that is, $c_{31} = 0.33$. Similar arguments can be used to determine the other transilient coefficients, which are sketched in Fig A1d. Thus, the transilient matrix for unequally-spaced grid points is ***asymmetric***, even when symmetric-type exchange mixing processes are occurring.

The definition of a transilient coefficient is a very specific "destination"-oriented definition: c_{ij} is the fraction of air in destination-grid-box i that came from source-grid-box j. This definition is still valid for unequally-spaced grid points and must be interpreted strictly; namely, c_{ij} is NOT the fraction of air in source-box j that left to go to box i. The first index always represents the destination, the second always represents the source, and the value of c is always taken with respect to the destination. Such a "destination" definition must be used in order for the prognostic equation to work: $S_i(t+\Delta t) = \Sigma_j \, c_{ij}(\Delta t) \, S_j$, which weights the various incoming tracer values by their relative contributions to the final total mass in the destination box.

With the strict definition of the transilient coefficients, each row of the transilient matrix must sum to unity:

$$1 = \sum_{j=1}^{n} c_{ij} \qquad \text{(A1)}$$

Physically, this is interpreted as ***air-mass conservation*** in the destination grid boxes. After mixing, each grid box is still filled with the same mass of air that it started with, and this air had to have come from somewhere. Fig A1d exemplifies this interpretation.

However, each column (which represents each source) does not necessarily sum to unity because of the "destination" definition of the transilient coefficients. If m_j and m_i represent the total masses of air within grid boxes j and i, respectively, then the fraction of air originally in source-box j that left to go to box i is $(m_i/m_j)\, c_{ij}$. Conservation of source material (ie., ***state conservation***) is now:

$$1 = \sum_{i=1}^{n} \frac{m_i}{m_j}\, c_{ij} \qquad \text{(A2)}$$

as is exhibited in Fig A1d. Both (A1) and (A2) are valid for any mixing process, even if there is not an equal exchange between the upper and lower grid points.

For the special case of perfect mass exchange as shown in Fig A1, the coefficients in the upper triangle of the matrix are related to those in the lower triangle by:

$$c_{ji} = \frac{m_i}{m_j}\, c_{ij} \qquad \text{(A3)}$$

where the first index of c always represents the destination. The mixing potential parameterization used in the body of this paper does not discriminate between upward and downward mixing, and thus is described by (A3).

b. A parameterization

The approach taken above to change from a large number of equal-size grid boxes to a smaller number of unequal-size boxes can be also used to parameterize the transilient coefficients as a function of mixing potentials, Y_{ij}. Consider, for example, the potential for mixing between each of the unit masses within box 4 (source) and the one unit mass within box 1 (destination). The potential for mixing between the unit mass *g* and unit mass *a* is Y_{ag} (=Y_{ga}). Similarly, the potentials between the other unit masses in 4 and the unit mass in 1 are Y_{ah}, Y_{ap}, and Y_{aq}. The total mixing potential between box 1 and all the unit masses in box 4 is the sum of all the individual potentials: $Y_{ag} + Y_{ah} + Y_{ap} + Y_{aq}$.

Mixing potentials, however, are determined by wind and temperature differences between the grid boxes according to (1). For the case of the column of 10 smaller grid boxes, we expect that each of the individual mixing potentials (Y_{ah}, etc.) could differ from each other corresponding to different winds and temperatures in those regions. However, for the case of the unequally-spaced coarser grid box, we know only one temperature and wind for the whole box, because anything smaller is unresolved subgrid scale. Thus, $Y_{ag} = Y_{ah} = Y_{ap} = Y_{aq} = Y_{14}$. As a result, the total mixing potential between boxes 1 and 4 is: $Y_{ag} + Y_{ah} + Y_{ap} + Y_{aq} = 4\, Y_{14}$. In general, the total mixing potential is $m_j\, Y_{ij}$, where we see that the mass of the source box is a weighting factor for the mixing potential.

A similar weighting does NOT occur for the destination boxes. For a coarse grid box, such as destination-box 4, 100% of the air mixing into any one of the smaller destination unit-mass boxes contributes only 25% to the total mass in box 4. Thus, the total contribution to the overall mixing into box 4 is $0.25\, Y_{ga} + 0.25\, Y_{ha} + 0.25\, Y_{pa} + 0.25\, Y_{qa}$. Because each of the mixing potentials for the smaller unit masses contained within box 4 are equal to Y_{41} (i.e., no subgrid differences), we find that the potential for mixing into box 4 is only Y_{41}, with no weighting by the mass of the destination box.

The row norm, RN_i, defines the total mixing potential within a row [see (2) in Section 2], and must include the source-mass weights as shown above. The single maximum row norm defines the maximum total mixing potential that can occur within a contiguous patch of turbulence, and is our definition of a matrix norm, $\|Y\|_\infty$ [see (3) in Section 2].

Our basic assumption for turbulence closure is: that the fraction of air mixed into a destination box from some source is proportional to the fraction of total mixing potential associated with that source/destination pair [described by (4a) in Section 2]. Because the row norms for each row (except one) are smaller than the matrix norm, that implies that those rows (destinations) have less total turbulent mixing into them than the one lucky destination. As a result, the no-mixing transilient coefficient (i.e., c_{ii}) is larger in those rows such that the sum of each row of transilient coefficients still equals unity [see (4b) in Section 2].

APPENDIX B

Implicit Tangent Filter

The set of symmetric low-pass implicit tangent filters of order 2p are defined by

$$[S^{2p}]u_n^F \; + \; (-1)^p \, \varepsilon [L^{2p}] u_n^F = [S^{2p}] u_n \quad . \tag{B1}$$

Here u_n^F is the filter variable while u_n is the unfiltered quantity. The parameter ε is the filter factor. In (B1) L^2u_n is the finite-difference analog of the second derivative of u at grid location n multiplied by the square of the grid step size, i.e., $L^2u_n = u_{n-1} - 2u_n + u_{n+1}$. Similarly, order 2p of the operator is analogous in the same way to a derivative of order 2p. The coefficients associated with the $(L)^{2p}$ operation are identical to those in the binomial expansion of $(a - b)^{2p}$. Also $S^2u_n = u_{n-1} + 2u_n + u_{n+1}$; consequently $(S/2)^2$ may be thought of as an averaging operator. The coefficients for $(S)^{2p}$ are the coefficients in the row with 2p+1 entries in Pascal's triangle.

The amplitude response of the implicit tangent filter of order 2p is given by

$$F(\kappa) = [\, 1 + \varepsilon \tan^{2p}(\kappa\delta/2)]^{-1} \, . \tag{B2}$$

Here δ is the grid step distance while κ is the wave number.

Figure Captions

Fig 1. Schematic of the vertical grid spacing of the sigma and half-sigma levels in the host Penn State/ NCAR mesoscale model. Temperature, moisture, and horizontal winds are at the half-sigma levels, while vertical velocity are at the full sigma levels.

Fig 2. Schematic (a) highlighting one element of a transilient matrix, and (b) indicating the associated nonlocal mixing between grid boxes in a column. The vertical distance between grid points 2 and 4 is also indicated.

Fig 3. Schematic vertical cross-section through a host model demonstrating vertical and horizontal turbulent mixing. The subset of grid boxes that participate in vertical mixing are indicated with (o). Those points that are also horizontal neighbors with other turbulent grid points can participate in horizontal mixing (shaded).

Fig 4. Schematic horizontal cross-section through a host model showing the horizontal-mixing stencil. For any grid point in the model (solid circle labeled: o), it is allowed to mix with only the subset of four or less immediate neighbors that are turbulent (solid circles labeled: 1 to 4).

Fig. 5. The filter response verses wave length $n\Delta x$ after 720 applications of the implicit tangent filter and the 4th order K theory diffusion in the Penn-State/NCAR regional model. The shaded region indicates the difference in response when using the minimum or maximum value allowed for K.

Fig. 6. The percent of the grid points turbulent as a function of time and pressure.

Fig. 7. The horizontal distribution of turbulence at (a) σ=.94 and (b) at σ=.74 twenty one hours into the forecast.

Fig. 8. Vertical cross sections of the (a) potential temperature (K) and (b) mixing ratio (kg kg^{-1}). Turbulence indicated by stipple.

Fig. 9. Mixing ratio (kg kg^{-1}) for the 15th sigma half level at forecast hour 48 for (a) TT with horizontal mixing, (b) TT without horizontal mixing and (c) for the control Penn State/NCAR model forecast. Contour interval is 0.1E-2 while the labels are scaled by 1.0E+4.

Fig. 10. The rms error in the 850 mb temperature (K) for the control forecast, for the standard Penn State/NCAR package of the Blackadar boundary layer formulation with K theory, with the Kuo cumulus parameterization and with explicit clouds. Also illustrated is the TT results with and without clouds.

Fig. 11. Mean error for the cases displayed in Fig. 7.

Fig. 12. Mean sea level pressure (mb) for (a) the control run with Kuo cumulus parameterization and (b) with explicit clouds. The TT parameterization scheme with explicit clouds is shown in (c). The verifying 48 h analysis is given in (d). Contour interval is 4 mb.

Fig. 13. The forecasted skin temperature, at hour 48, for the control (a) and for (b) the TT formulation. Both are for explicit cloud calculations. Contour interval is 3 K.

Fig. 14. Omega norm as a function of time. Note the difference between the control and the TT forecasts. Influence of allowing the viscous layer coefficient c_3 to vary in time (Var) and of explicit cloud calculations (clouds) are also illustrated.

Fig. 15 Cumulative rain and evaporation for the 72 hr forecasts with (Exp) and without (Reg) explicit clouds. Explicit cloud calculations contain the influence of the feedback mechanisms of rainwater evaporation and water loading. Allowing c_3 to vary (Var) reduces the rainfall in the TT forecasts.

Fig. 16 Omega norm as a function of time for the CAPTEX case. Note the diurnal variation for the TT parameterization cases.

Fig. 17 Omega norm (CAPTEX) showing the influences of feedback processes. In (a) the effects on the TT forecasts are illustrated while (b) outlines the results in the control forecasts.

Fig. 18 The change in the hourly forecasted precipitation is shown for the TT forecast (CAPTEX) and for the convective and large scale components of precipitation in the control forecast.

Fig. 19 Satellite IR images showing cloud cover at (a) 2100 UTC 25 September 1983 and for (b) 0000 , (c) 0300 and (d) 0600 UTC 26 September 1983.

Fig. 20 Horizontal fields of omega (CAPTEX) at the 8th sigma level 36 hrs into the forecast (0000 UTC 26 September 1983) for (a) TT and (b) for the control. Contour interval is 0.15E-3 while labels are scaled by 0.1E+6. Dashed lines indicate upward motion.

Fig. 21 The accumulated rainfall is shown as a function of time for the TT forecast and the large scale and convective components of the precipitation in the control forecast.

Fig. 22 Cumulative rainfall and evaporation for TT with (Exp) and without explicit clouds (Reg), with no horizontal mixing (No Horiz), and for the control with Kuo cumulus parameterization and with explicit clouds.

Fig. 23 Comparison of the heat-flux (a) and moisture-flux (b), given in units of W m^{-2}, between TT and the control at grid location (x_{25},y_{25}). The TT heat and moisture flux is for the surface and sigma level 15 while for the control we present both values.

Fig. 24 Bias scores in rainfall (CAPTEX) measuring the accuracy of the coverage of the rainfall after 72 hours.

Fig. 25. The 850 mb (a) rms and (b) mean error in the geopotential heights for the control (Blackadar) and TT approach, with and without explicit clouds.

Fig A1. (a) Schematic of a column of 10 equally-spaced grid points labeled a - q, each representing a unit mass of air contained within the grid boxes drawn. For sake of demonstration, assume that air is completely removed from some grid boxes and replaced by air from other grid boxes, as indicated by the arrows.

(b) Symmetric transilient matrix corresponding to (a). Note that this matrix is shown upside-down, so that each row of the matrix corresponds to the associated height of the grid box of part (a). The main diagonal is highlighted by a shaded line, and zero elements are left blank. Each row and column of the matrix sums to one.

(c) Schematic of a column of 4 unequally-spaced grid points based on groupings of the unit masses from (a). The same amount of mass exchange as (a) is assumed to occur, as indicated by the arrows.

(d) Asymmetric transilient matrix corresponding to (c). Each row sums to one, but each column does not.

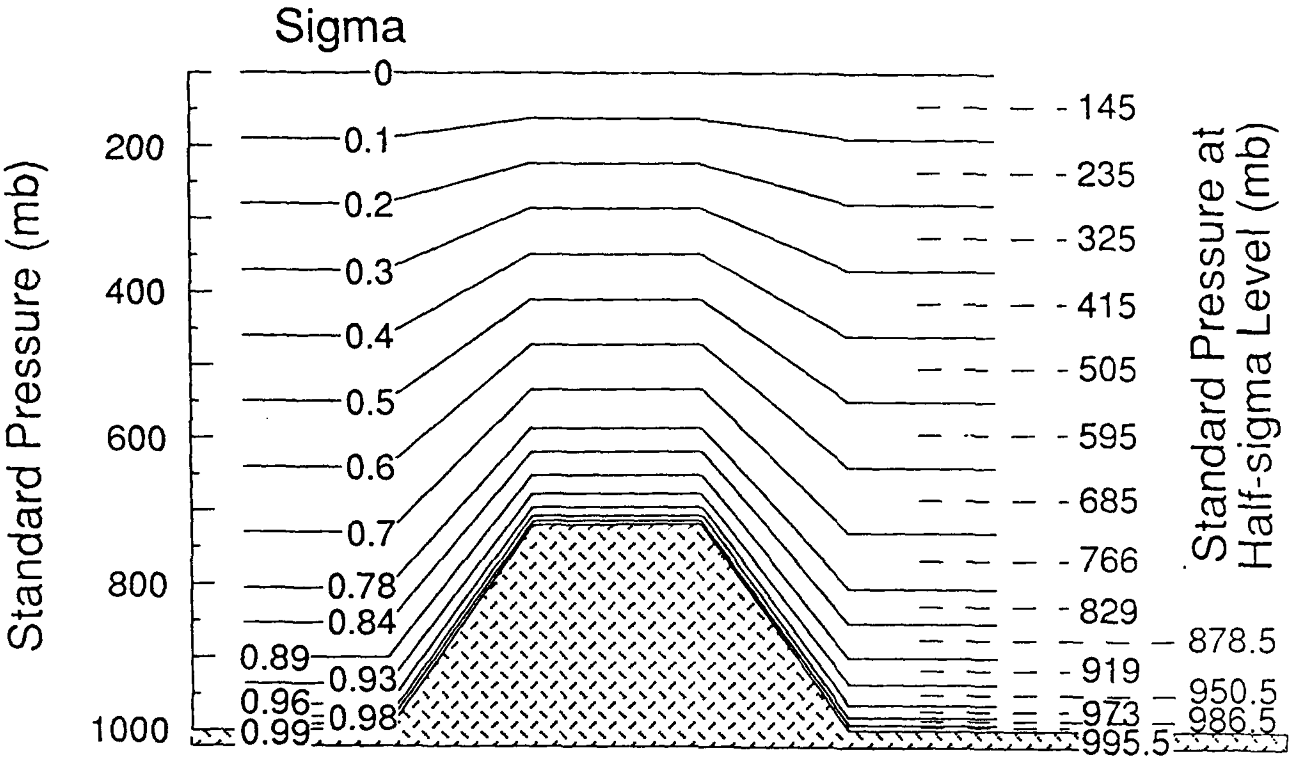
Sigma
0
0.1
0.2
0.3
0.4
0.5
0.6
0.7
0.78
0.84
0.89
0.93
0.96
0.98
0.99
Standard Pressure (mb)
200
400
600
800
1000
145
235
325
415
505
595
685
766
829
878.5
919
950.5
973
986.5
995.5
Standard Pressure at Half-sigma Level (mb)

FIGURE 1

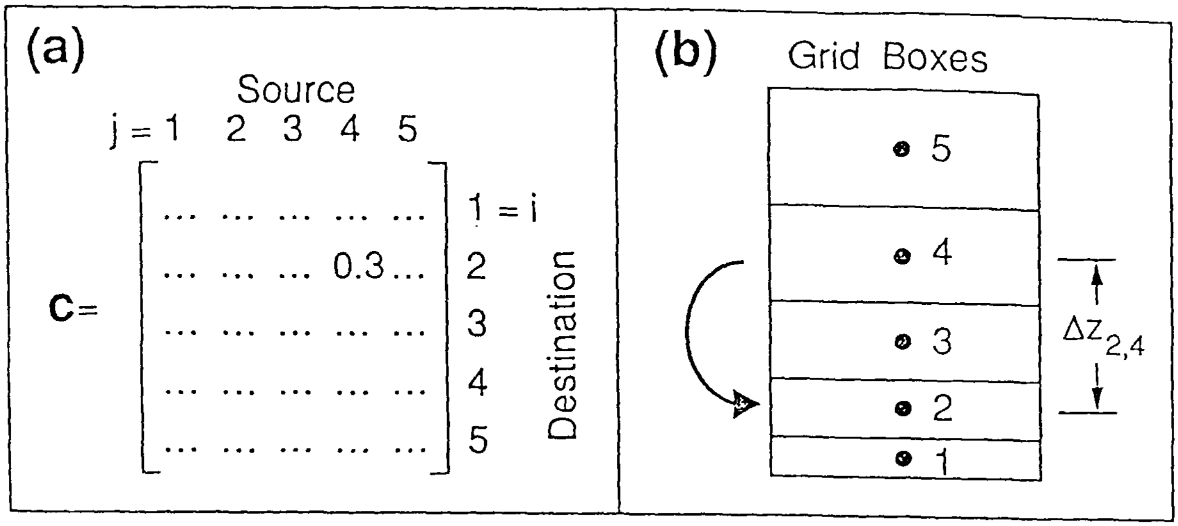

FIGURE 2

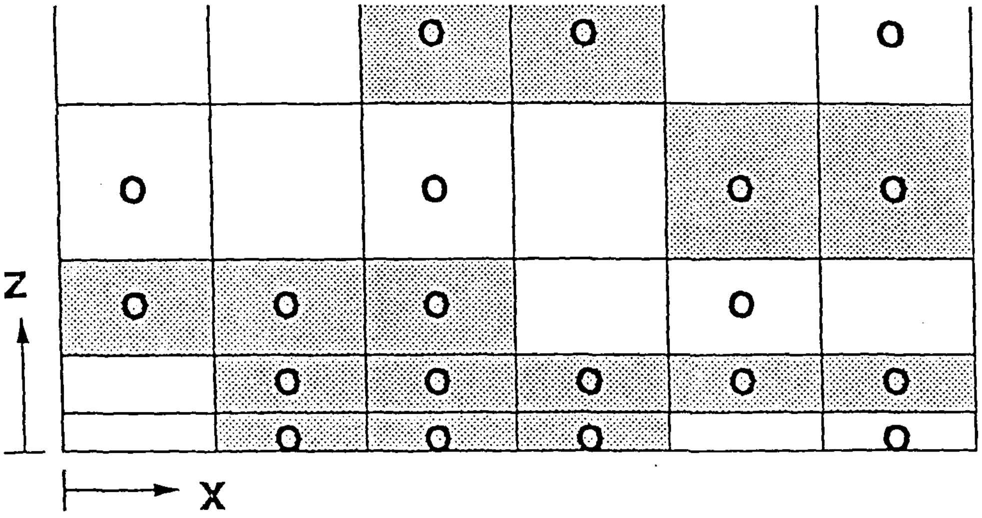

FIGURE 3

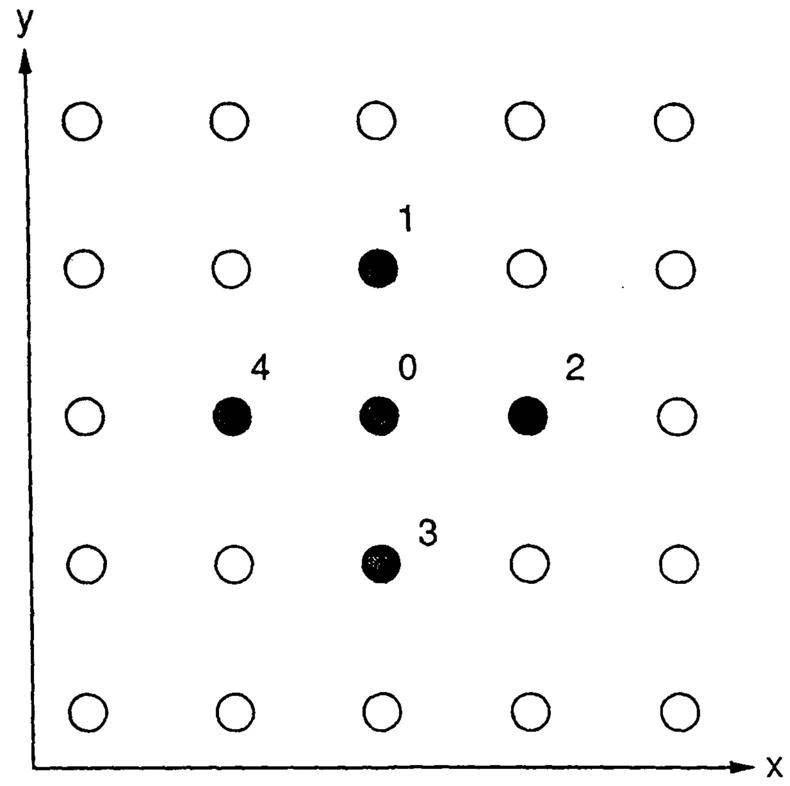

FIGURE 4

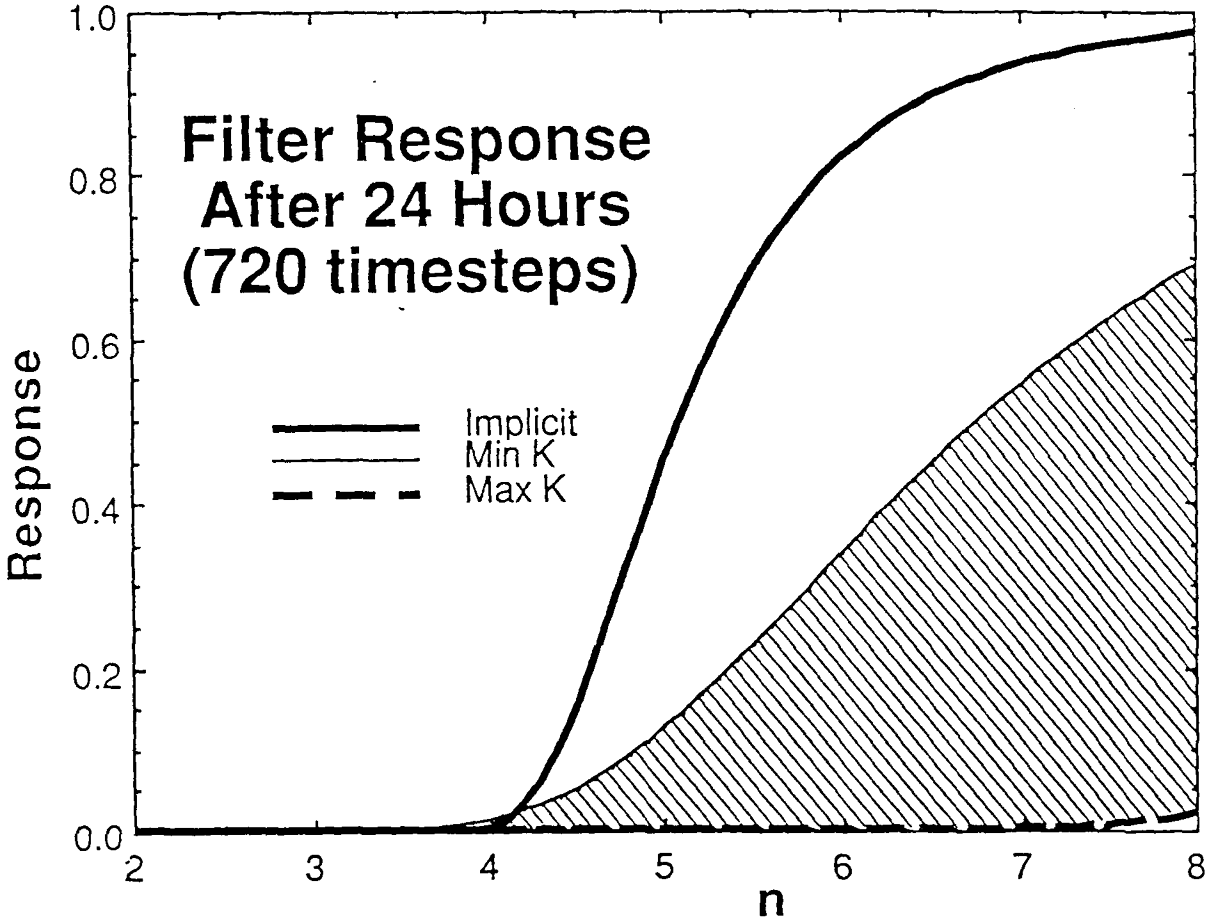
Filter Response
After 24 Hours
(720 timesteps)
Response
n
Implicit
Min K
Max K
0.0
0.2
0.4
0.6
0.8
1.0
2
3
4
5
6
7
8

FIGURE 5

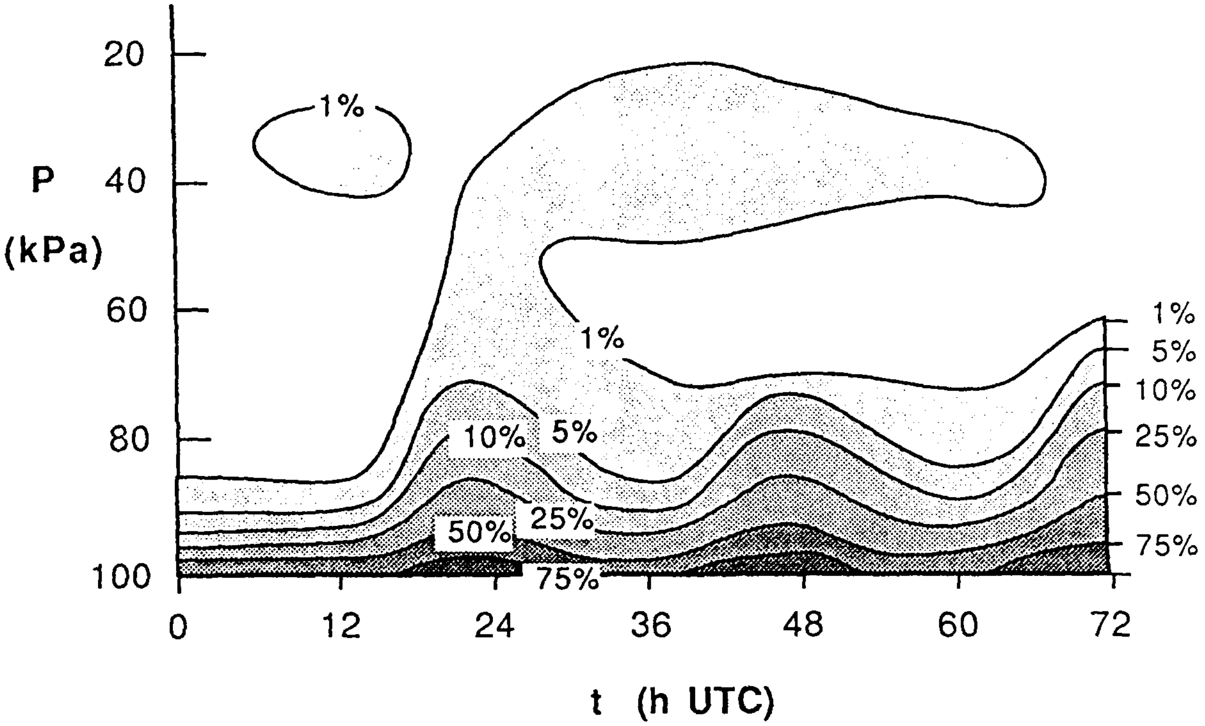
P
(kPa)
20
40
60
80
100
0
12
24
36
48
60
72
t (h UTC)
1%
1%
5%
10%
25%
50%
75%
1%
5%
10%
25%
50%
75%

FIGURE 6

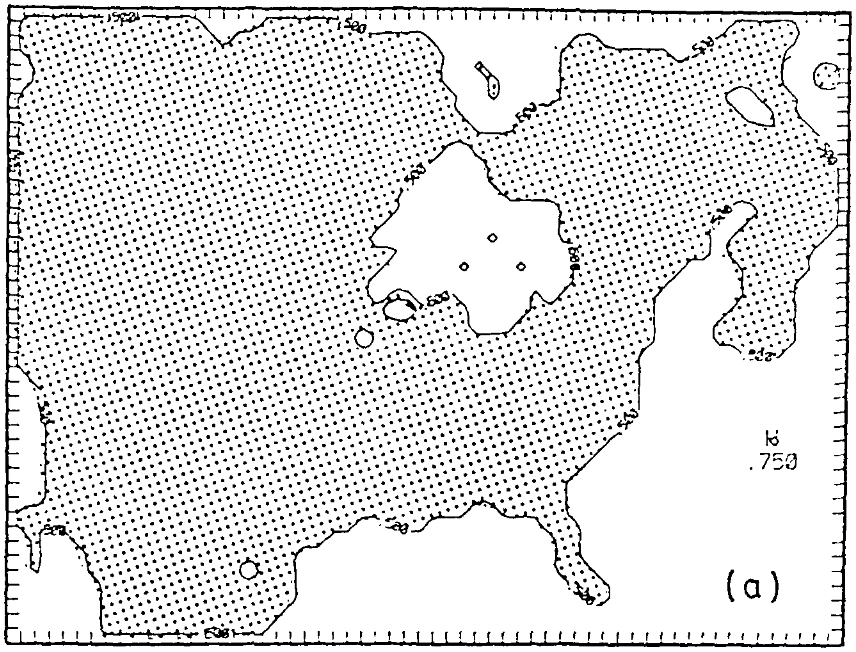

CONTOUR FROM 0.00000 TO 0.50000 CONTOUR INTERVAL OF 0.50000 PT(3,3)= 0.00000

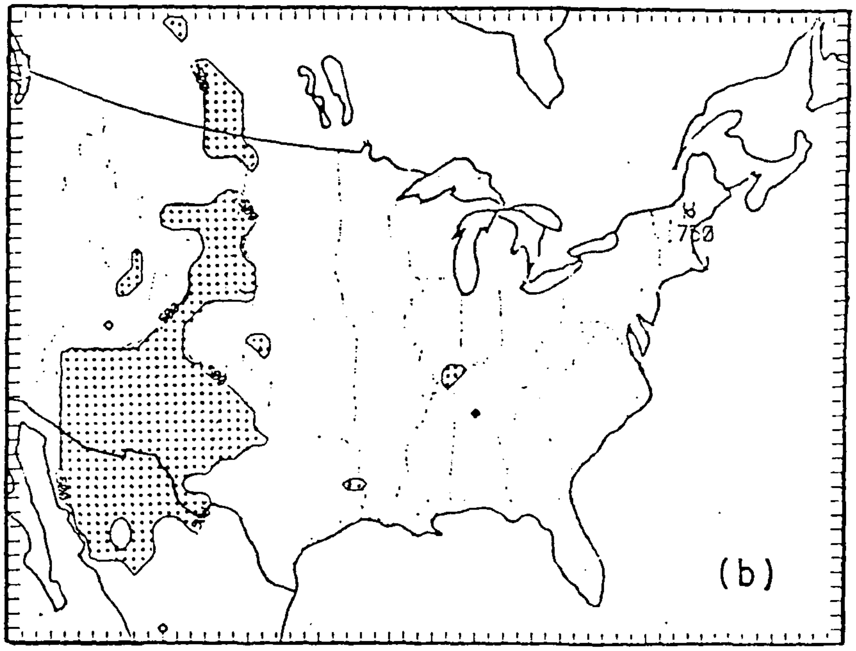

CONTOUR FROM 0.00000 TO 0.50000 CONTOUR INTERVAL OF 0.50000 PT(3,3)= 0.00000

FIGURE 7

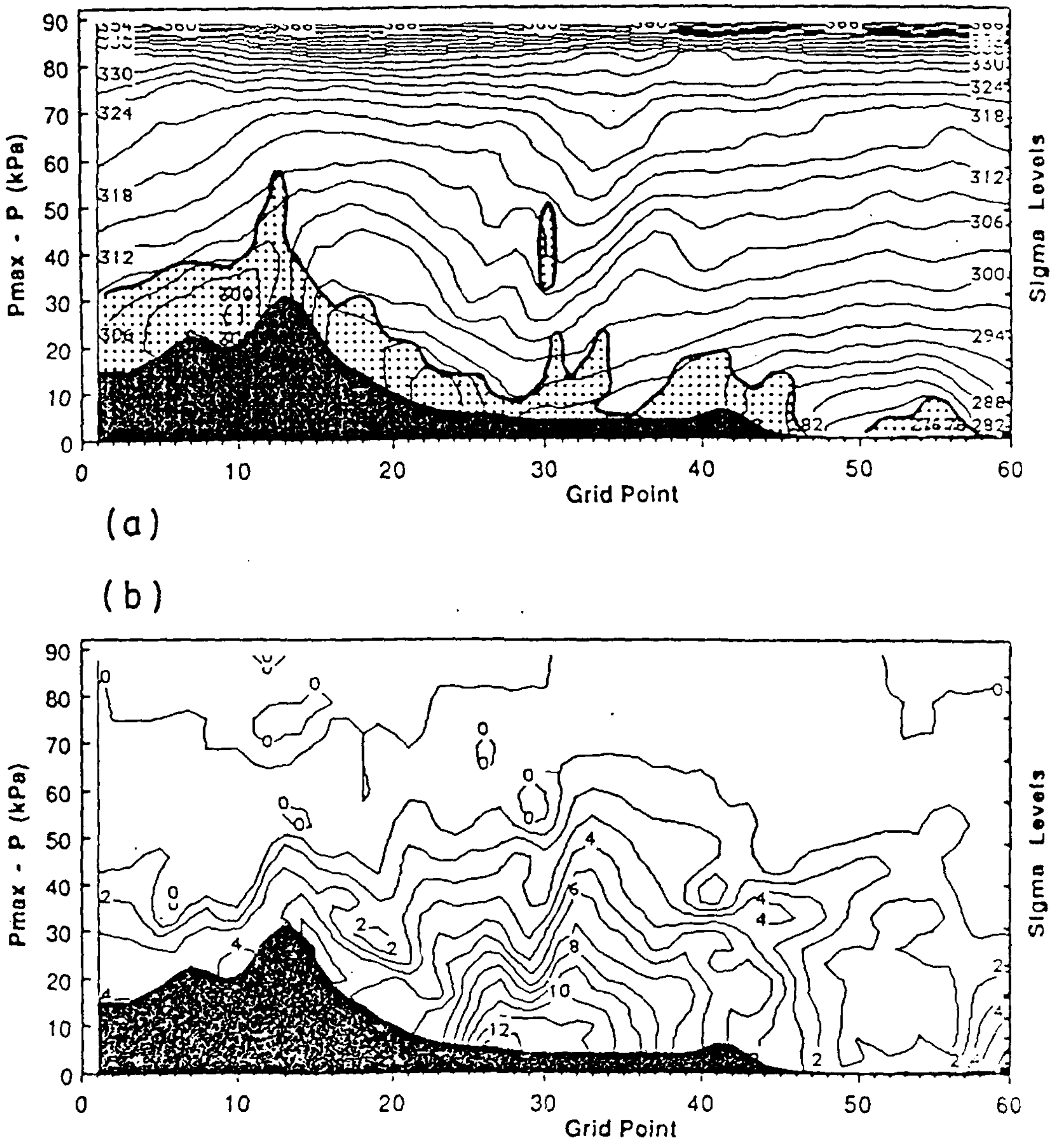Pmax - P (kPa)
Sigma Levels
Grid Point
(a)
(b)
330
324
318
312
306
300
294
288
282
0
2
4
6
8
10
12
0
10
20
30
40
50
60
70
80
90

FIGURE 8

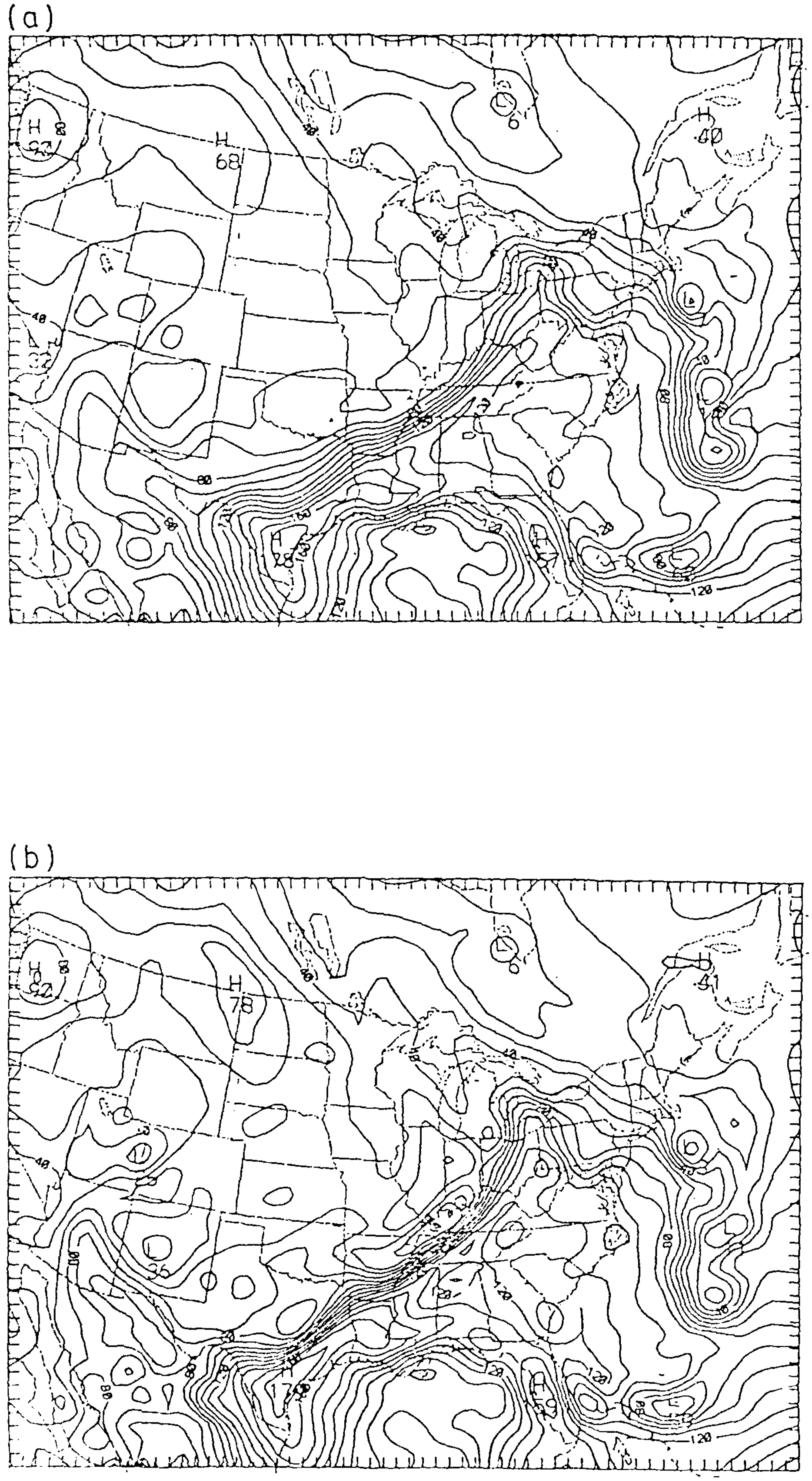

FIGURE 9

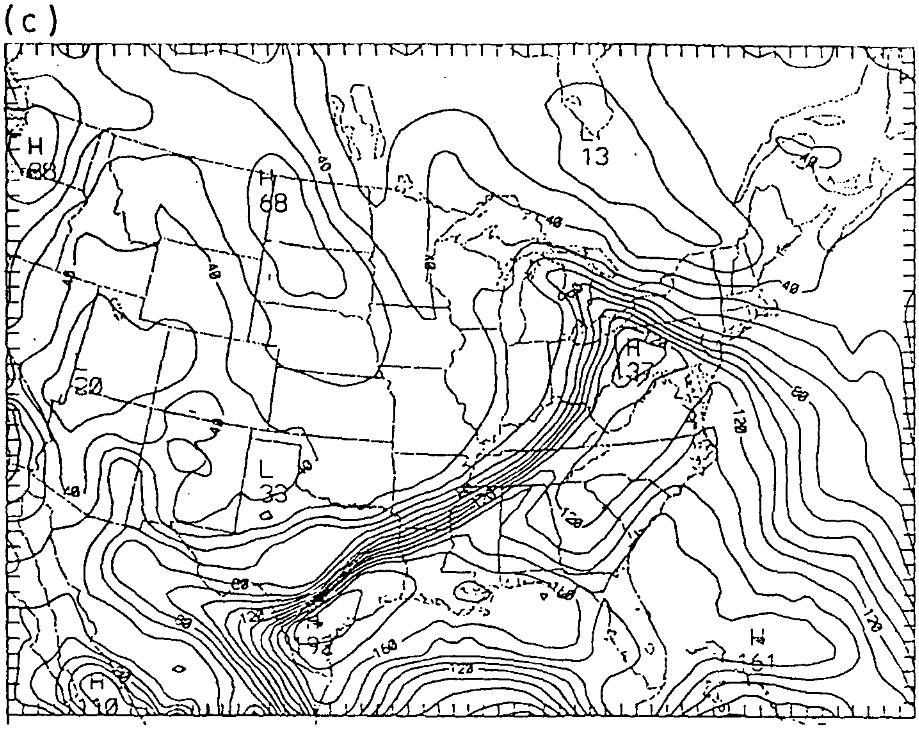

FIGURE 9 (Cont)

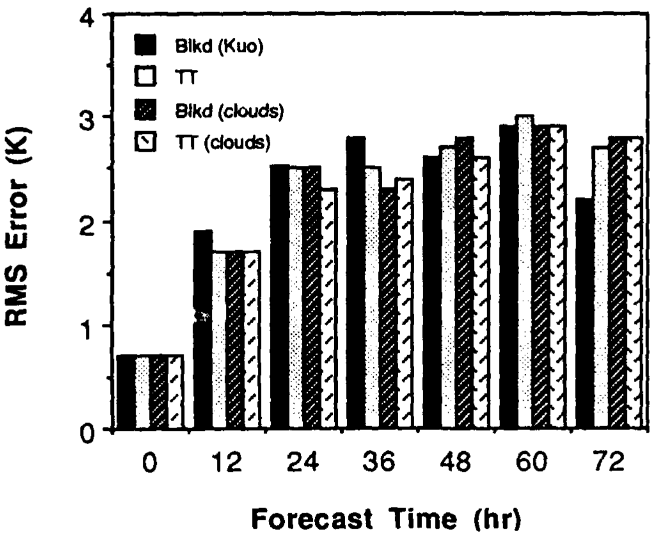

FIGURE 10

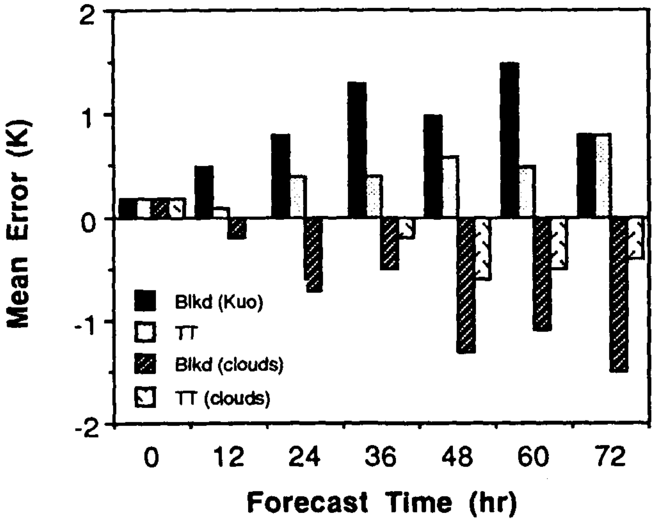

FIGURE 11

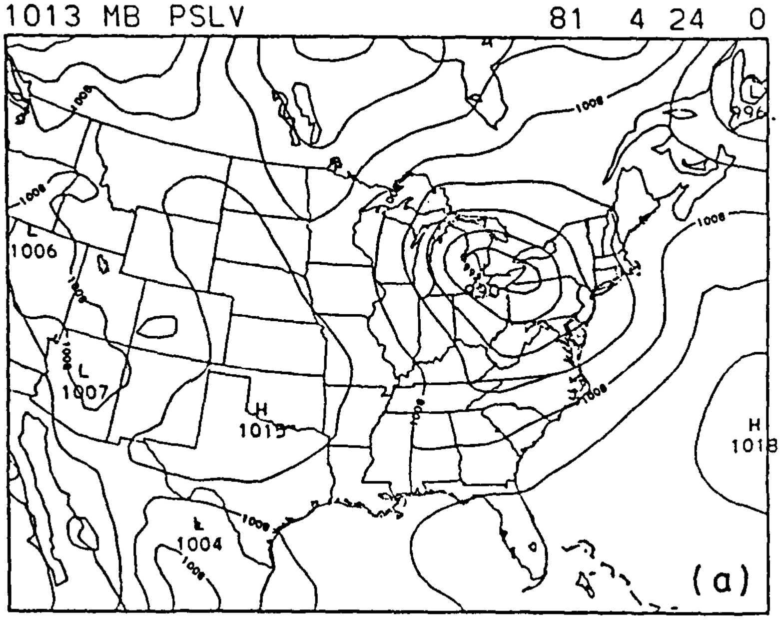

BLACKADAR VS ANALYSIS

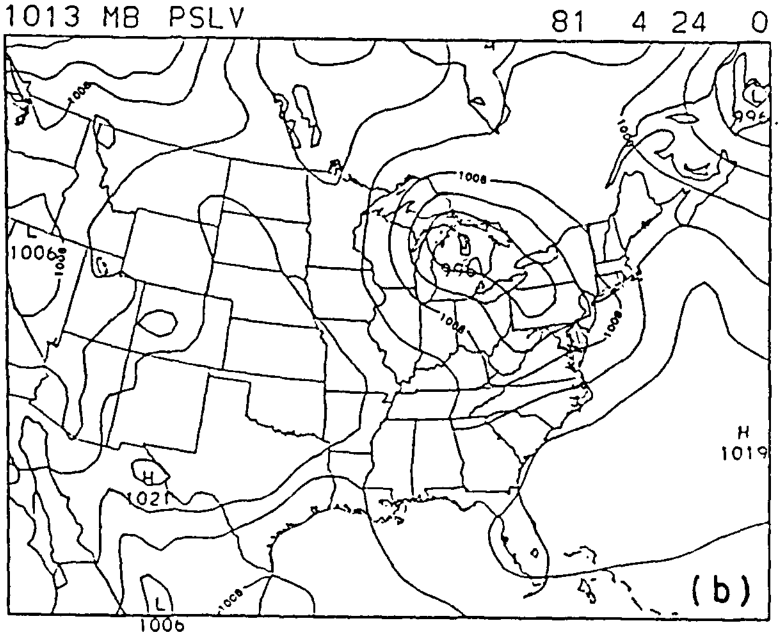

BLACKADAR VS ANALYSIS

FIGURE 12

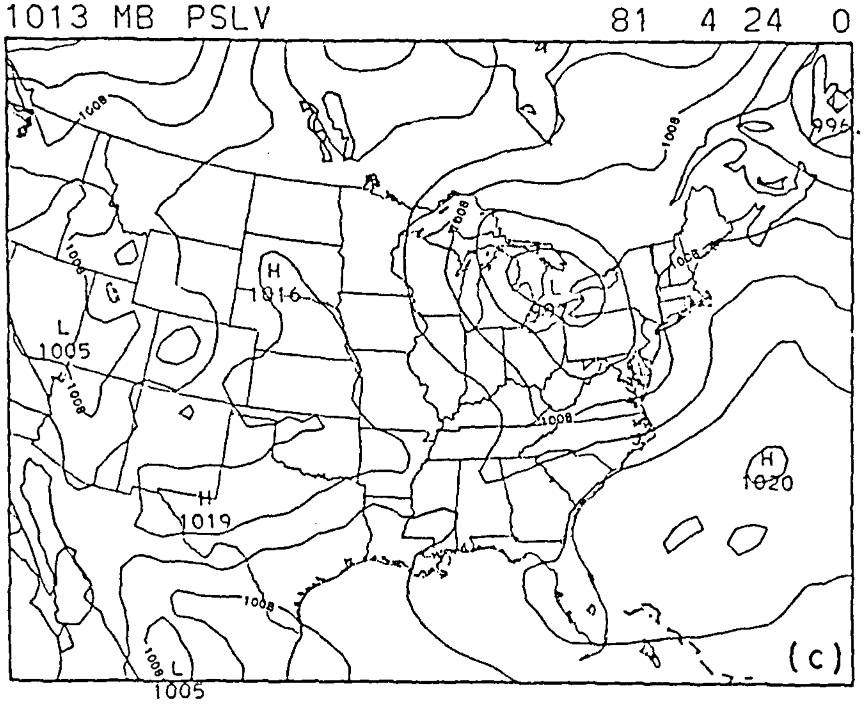

TRANSILIENT VS ANALYSIS

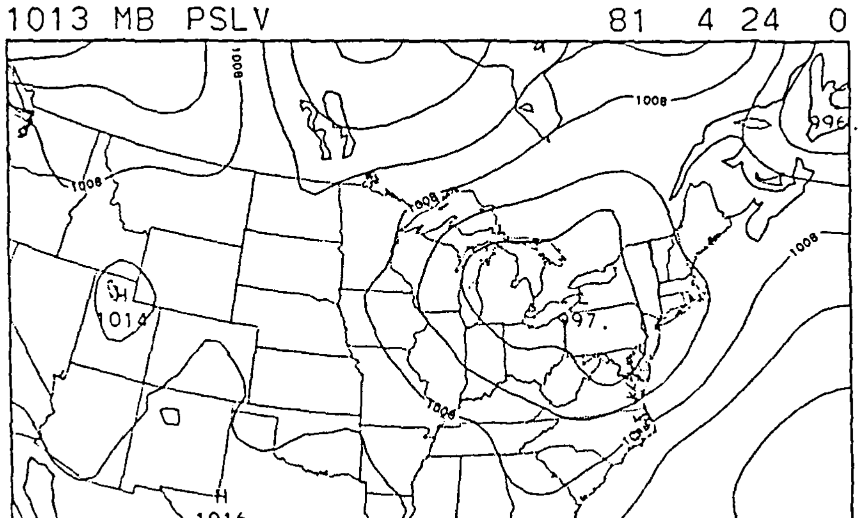

FIGURE 12 (Cont)

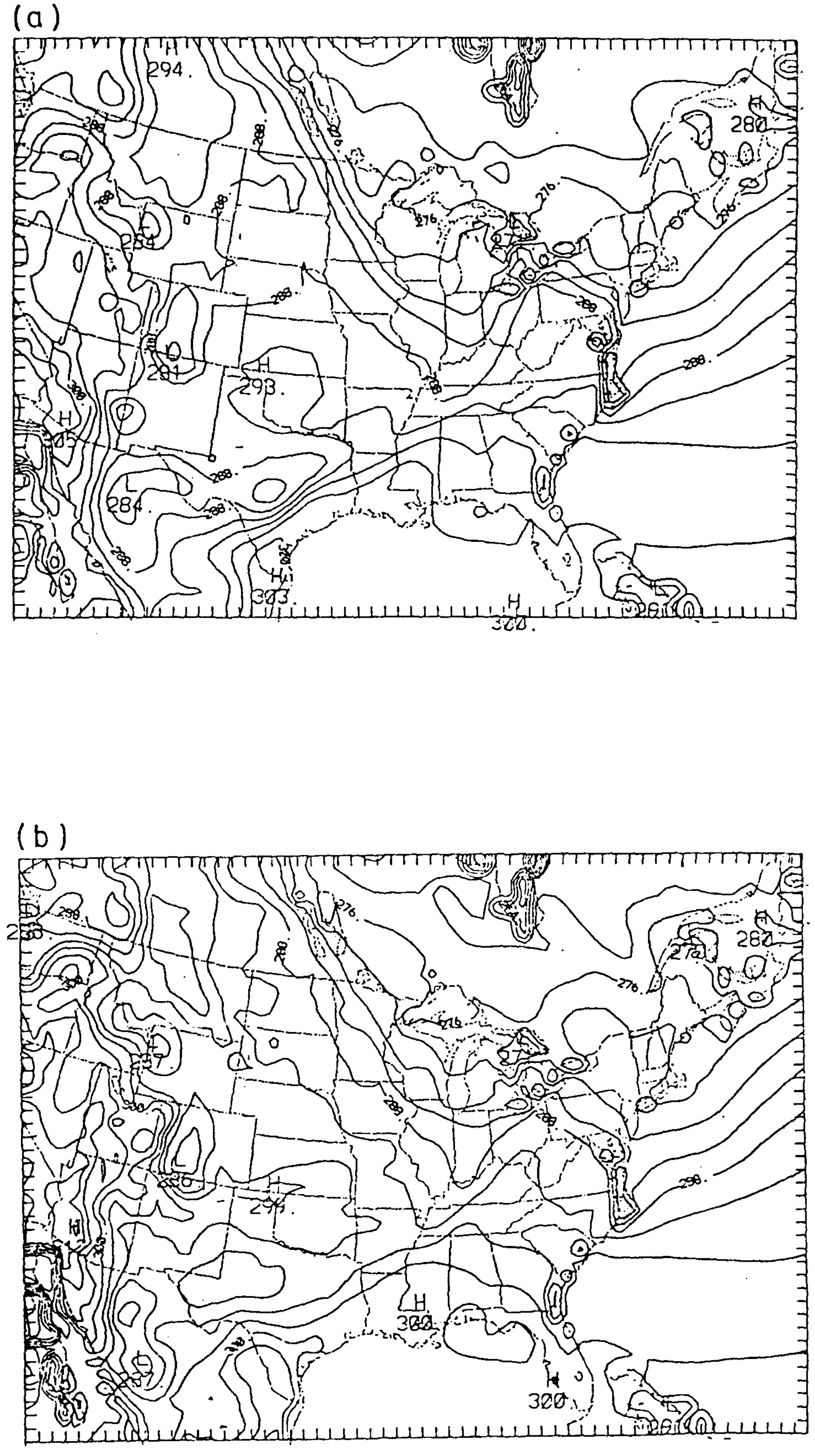
(a)
H
294.
H
280
276
288
281
H
293.
H
305
L
284
288
H
303.
H
300.
281
(b)
298
276
280
282
300
H
294.
H
300
H
300.
281

FIGURE 13

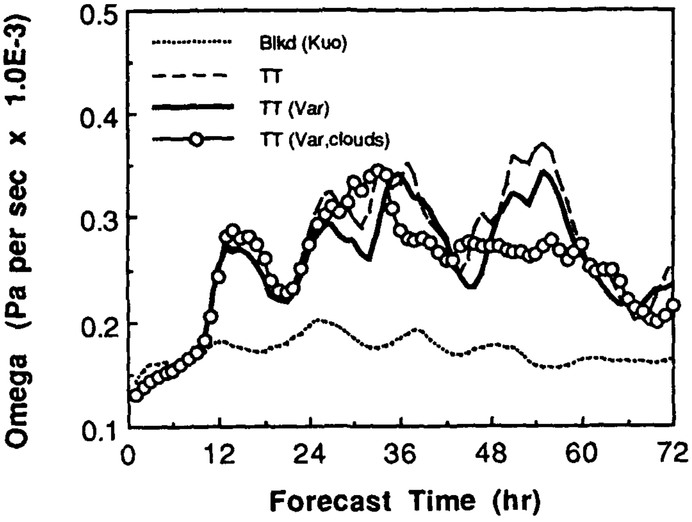

FIGURE 14

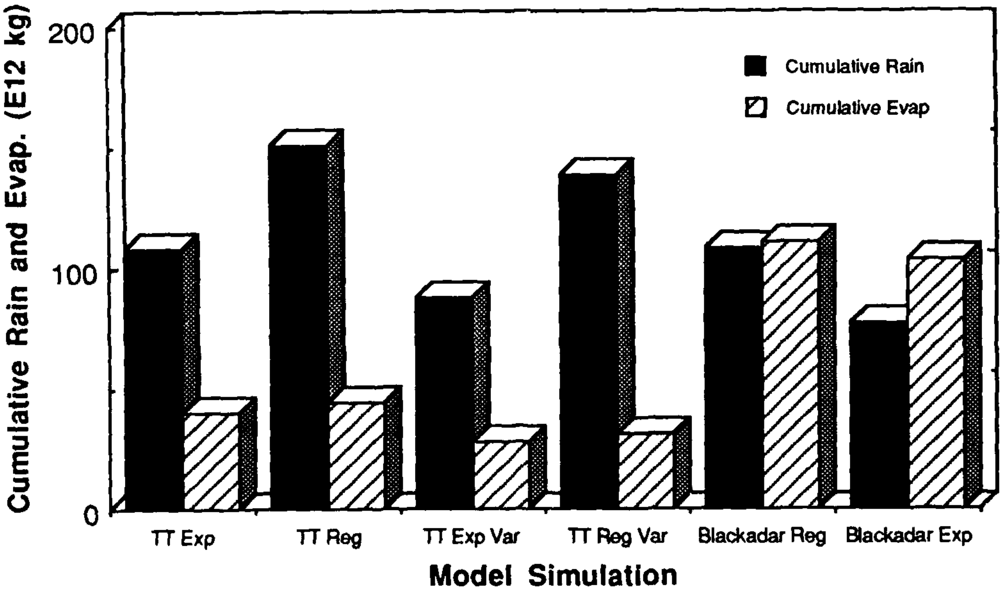

FIGURE 15

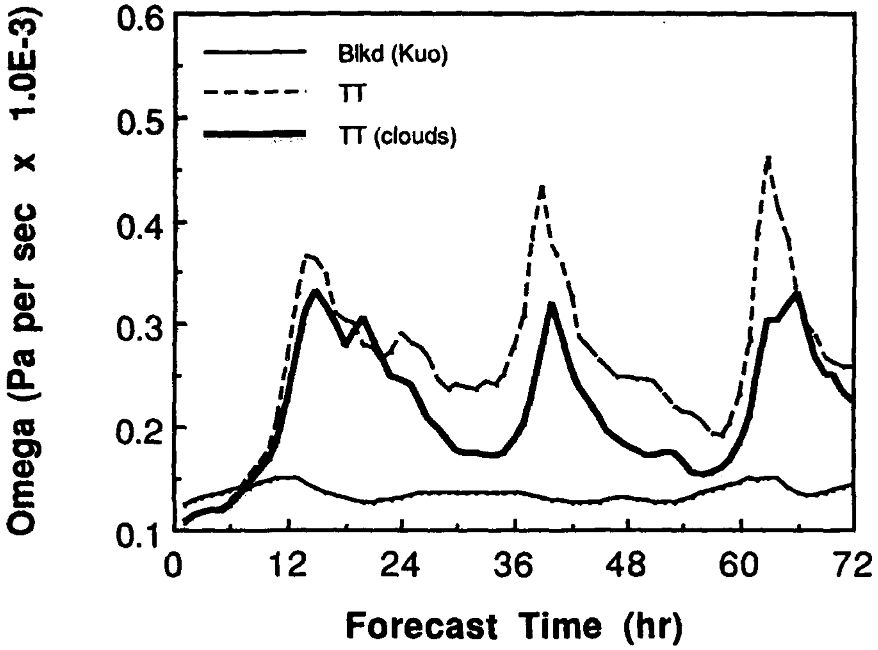
Omega (Pa per sec x 1.0E-3)
0.6
0.5
0.4
0.3
0.2
0.1
0
12
24
36
48
60
72
Forecast Time (hr)
Blkd (Kuo)
TT
TT (clouds)

FIGURE 16

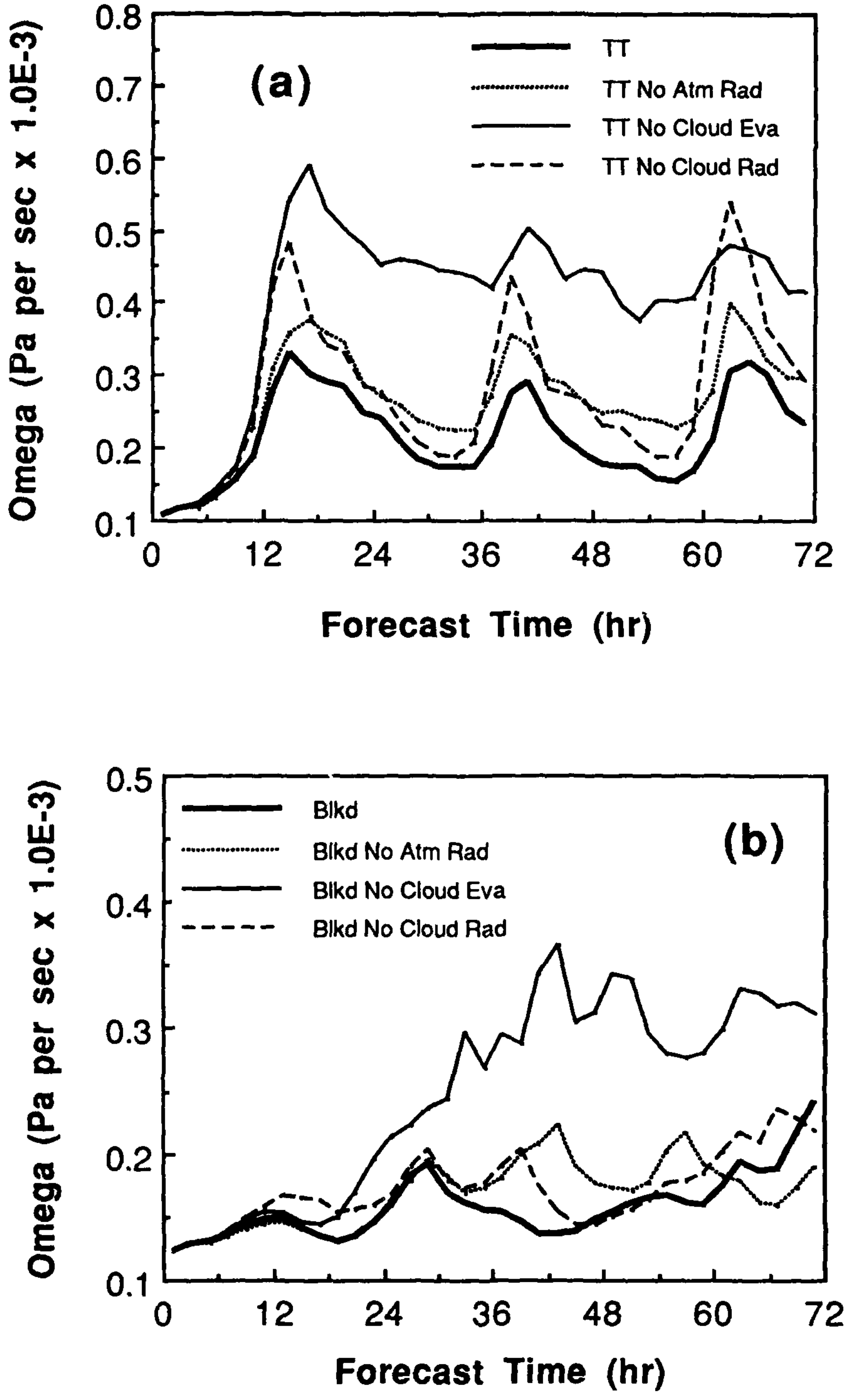
(a)
TT
TT No Atm Rad
TT No Cloud Eva
TT No Cloud Rad
Omega (Pa per sec x 1.0E-3)
0.8
0.7
0.6
0.5
0.4
0.3
0.2
0.1
0
12
24
36
48
60
72
Forecast Time (hr)
(b)
Blkd
Blkd No Atm Rad
Blkd No Cloud Eva
Blkd No Cloud Rad
Omega (Pa per sec x 1.0E-3)
0.5
0.4
0.3
0.2
0.1
0
12
24
36
48
60
72
Forecast Time (hr)

FIGURE 17

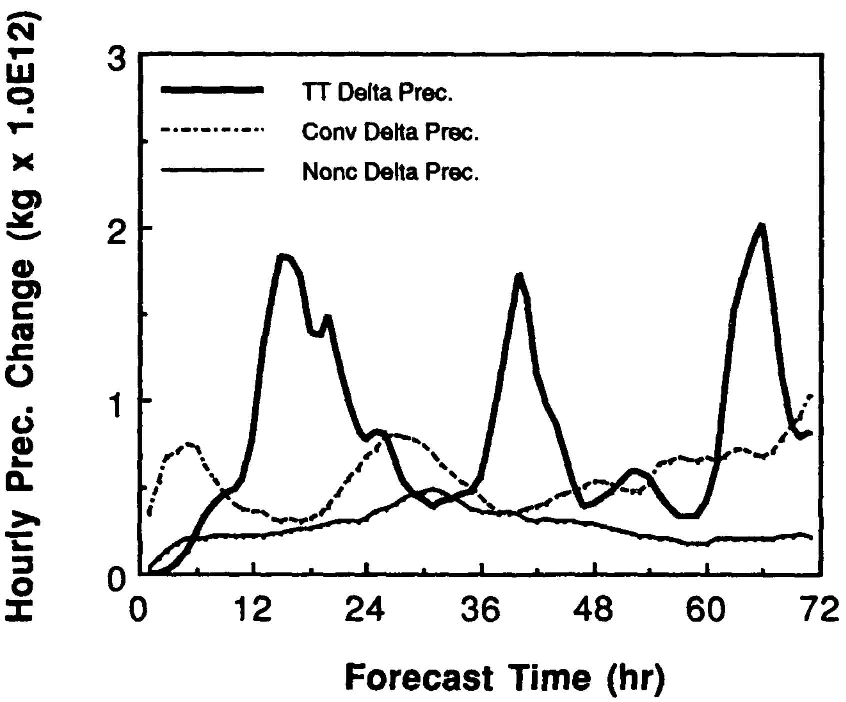
Hourly Prec. Change (kg x 1.0E12)
3
2
1
0
0
12
24
36
48
60
72
Forecast Time (hr)
TT Delta Prec.
Conv Delta Prec.
Nonc Delta Prec.

FIGURE 18

FIGURE 19a

FIGURE 19b

FIGURE 19c

FIGURE 19d

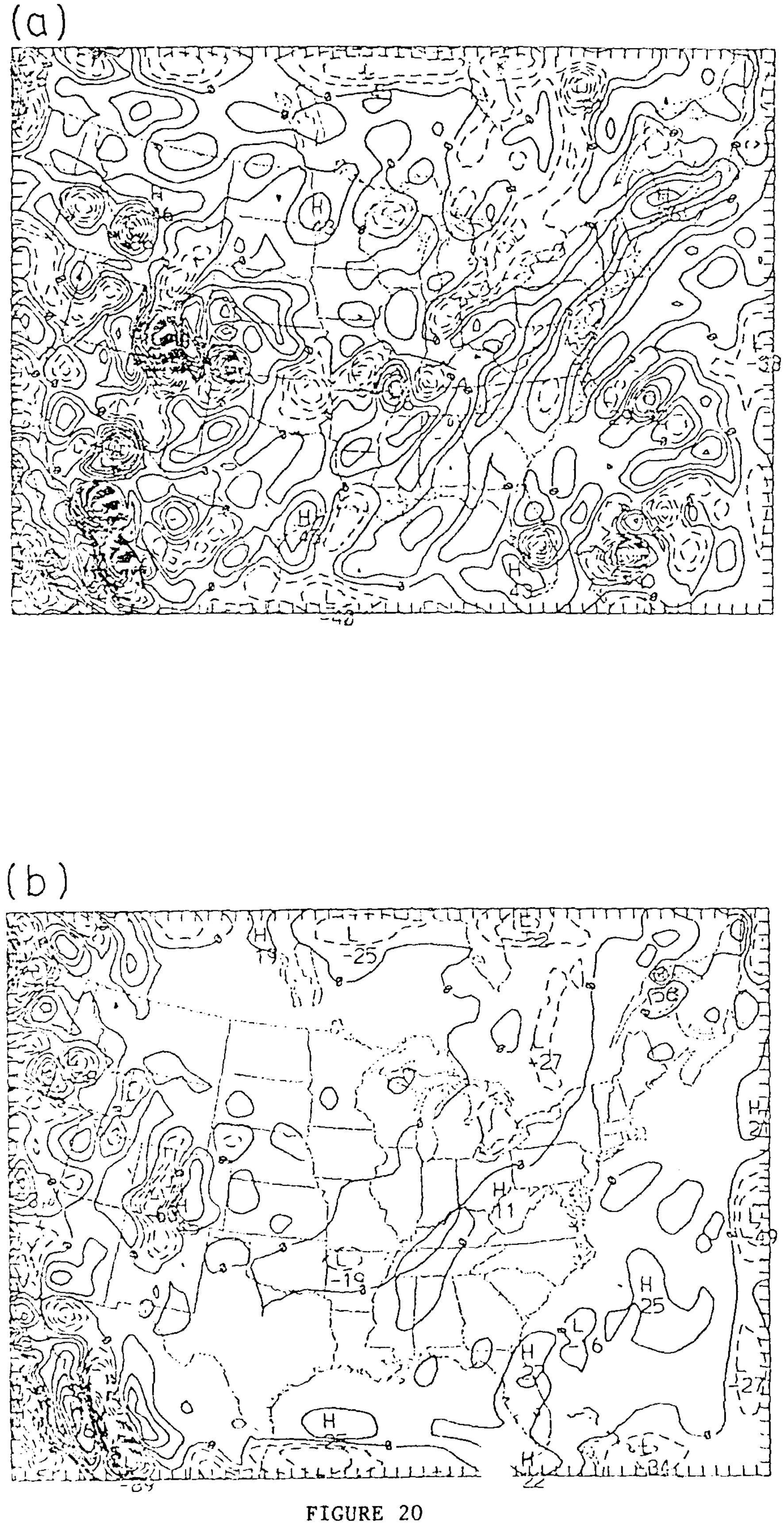

FIGURE 20

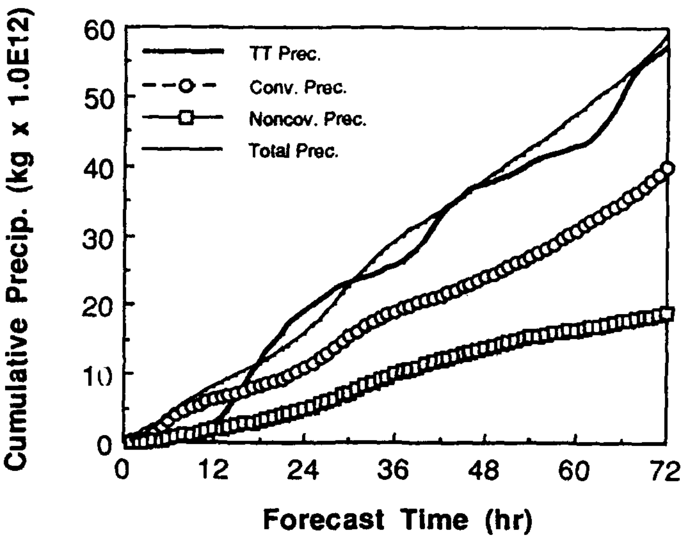

FIGURE 21

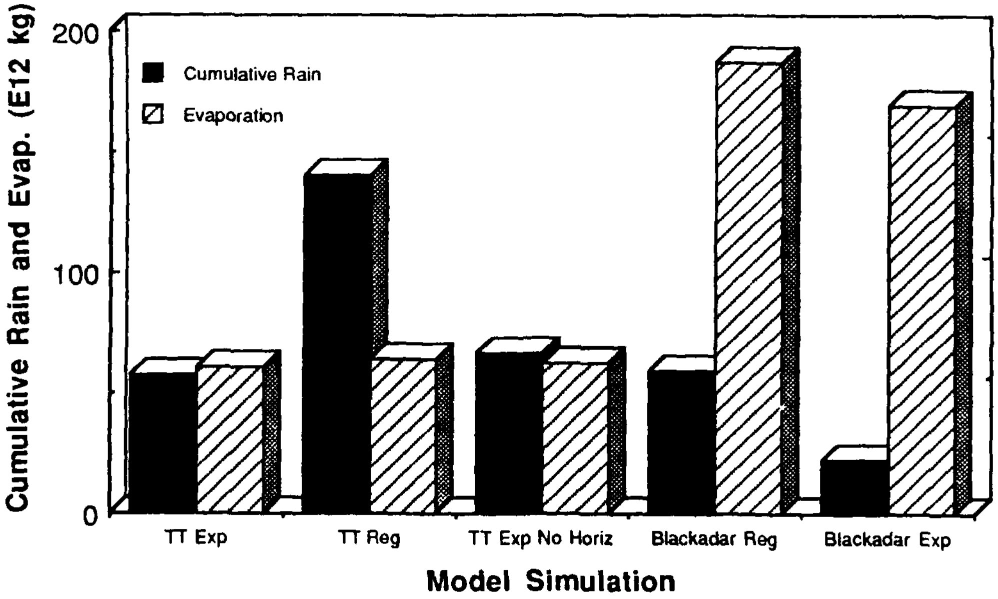

FIGURE 22

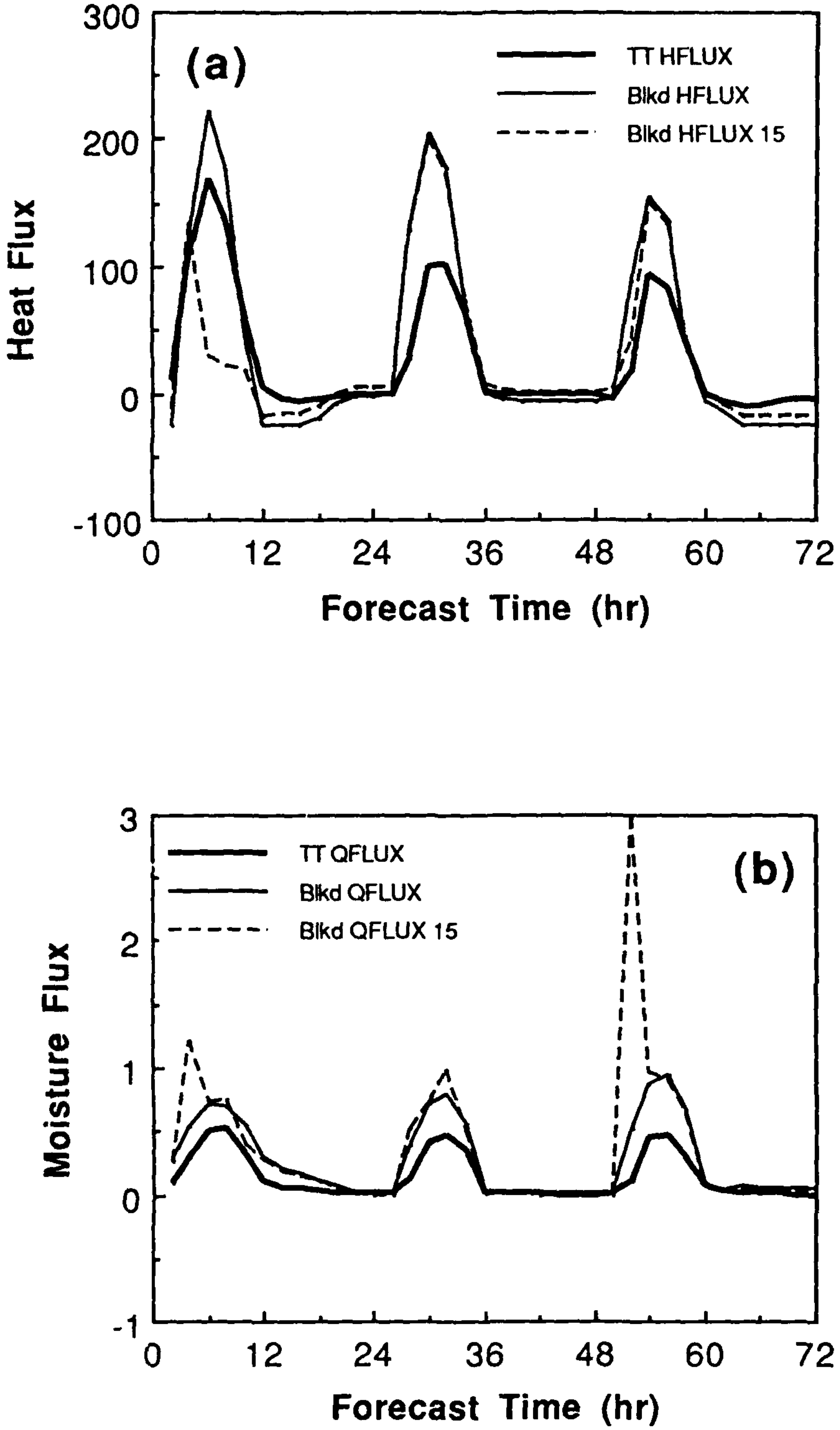
(a)
TT HFLUX
Blkd HFLUX
Blkd HFLUX 15
Heat Flux
300
200
100
0
-100
0
12
24
36
48
60
72
Forecast Time (hr)
(b)
TT QFLUX
Blkd QFLUX
Blkd QFLUX 15
Moisture Flux
3
2
1
0
-1
0
12
24
36
48
60
72
Forecast Time (hr)

FIGURE 23

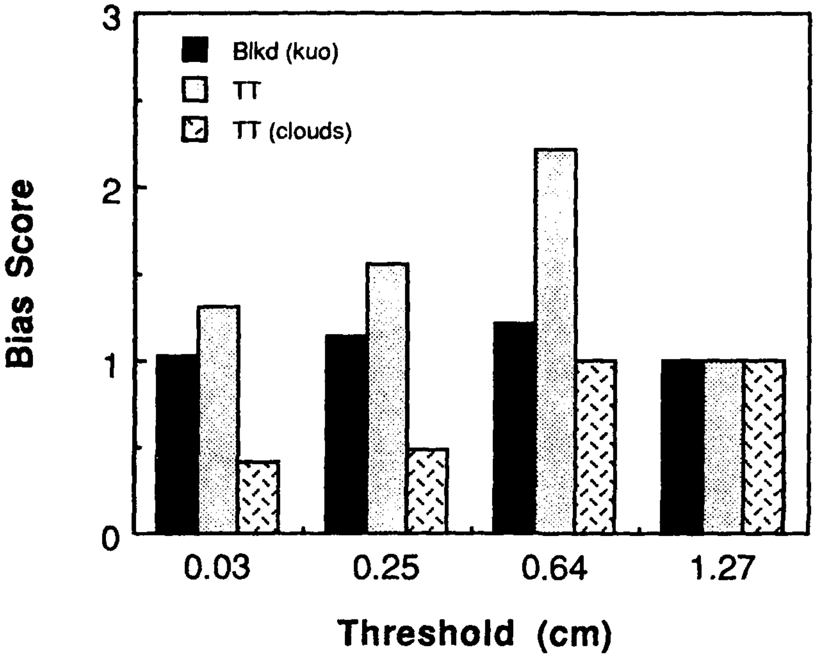

Bias Score
3
2
1
0
■ Blkd (kuo)
□ TT
▨ TT (clouds)
0.03
0.25
0.64
1.27
Threshold (cm)

FIGURE 24

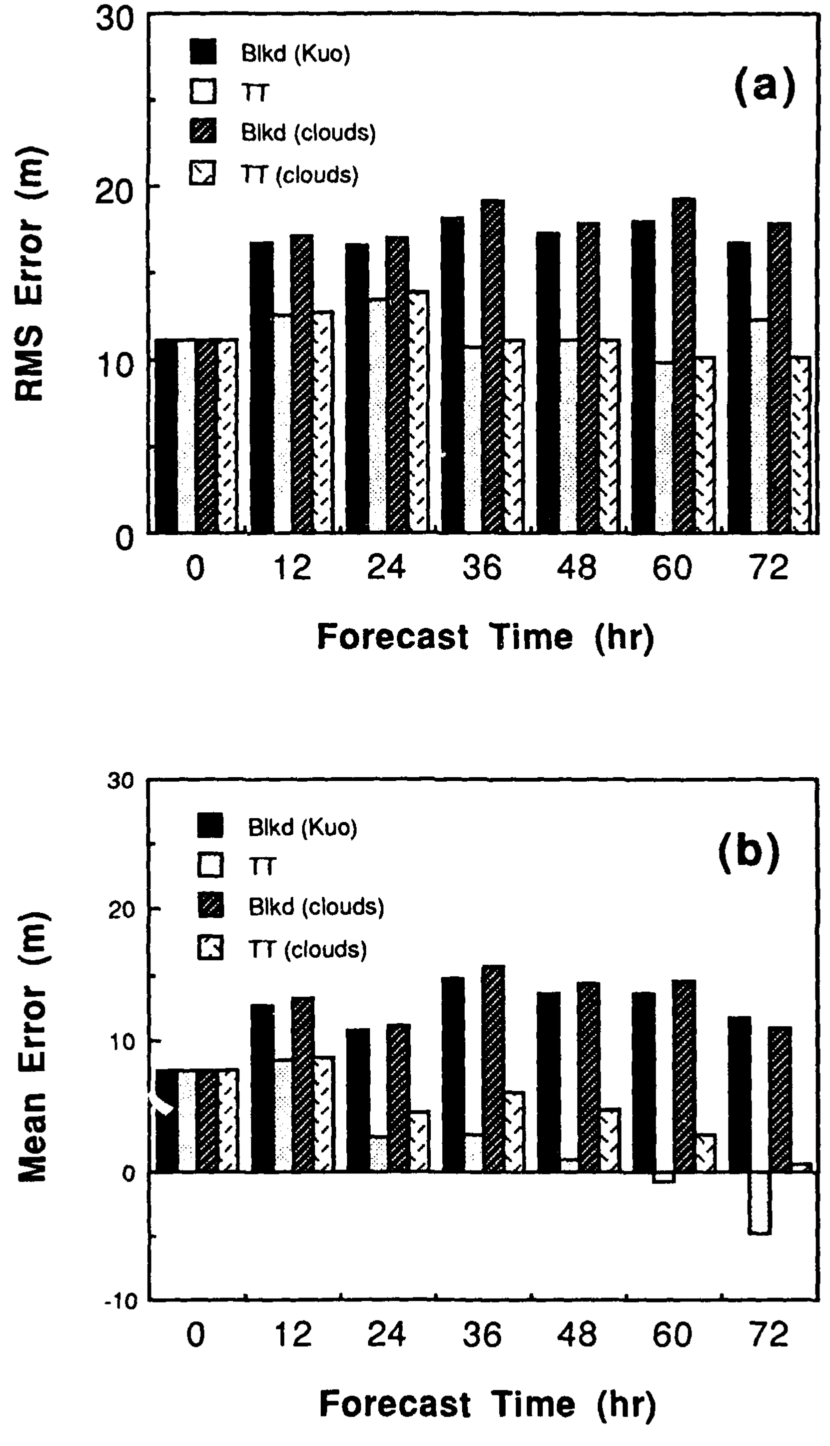
(a)
Blkd (Kuo)
TT
Blkd (clouds)
TT (clouds)
RMS Error (m)
0
10
20
30
0
12
24
36
48
60
72
Forecast Time (hr)
(b)
Blkd (Kuo)
TT
Blkd (clouds)
TT (clouds)
Mean Error (m)
-10
0
10
20
30
0
12
24
36
48
60
72
Forecast Time (hr)

FIGURE 25

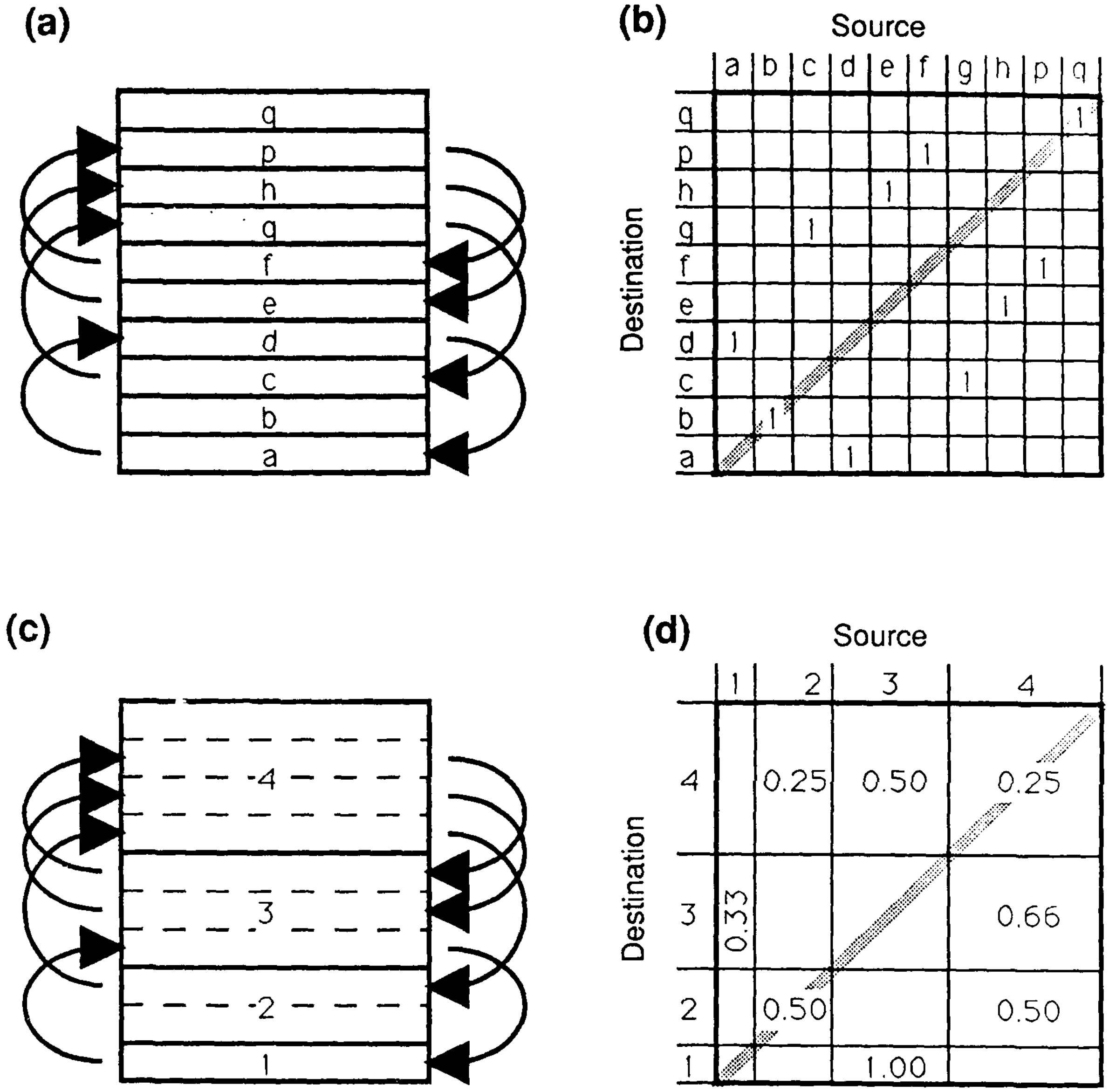

(b)

Destination \ Source	a	b	c	d	e	f	g	h	p	q
q										1
p						1				
h					1					
g			1							
f									1	
e								1		
d	1									
c							1			
b		1								
a				1						

(d)

Destination \ Source	1	2	3	4
4		0.25	0.50	0.25
3	0.33			0.66
2		0.50		0.50
1			1.00	

FIGURE A1